Mon. Not. R. Astron. Soc. **398,** 1793–1808 (2009) doi:10.1111/j.1365-2966.2009.15267.x

An AzTEC 1.1 mm survey of the GOODS-N field – II. Multiwavelength identifications and redshift distribution

Edward L. Chapin,[1★] Alexandra Pope,[2†] Douglas Scott,[1] Itziar Aretxaga,[3] Jason E. Austermann,[4] Ranga-Ram Chary,[5] Kristen Coppin,[6] Mark Halpern,[1] David H. Hughes,[3] James D. Lowenthal,[7] Glenn E. Morrison,[8,9] Thushara A. Perera,[10] Kimberly S. Scott,[4] Grant W. Wilson[4] and Min S. Yun[4]

[1]*Department of Physics & Astronomy, University of British Columbia, 6224 Agricultural Road, Vancouver, BC V6T 1Z1, Canada*
[2]*National Optical Astronomy Observatory, 950 N. Cherry Ave., Tucson, AZ 85719, USA*
[3]*Instituto Nacional de Astrofísica, Óptica y Electrónica (INAOE), Aptdo. Postal 51 y 216, Puebla, Mexico*
[4]*Department of Astronomy, University of Massachusetts, Amherst, MA 01003, USA*
[5]*Division of Physics, Mathematics, and Astronomy, California Institute of Technology, Pasadena, CA 91125, USA*
[6]*Institute for Computational Cosmology, University of Durham, South Road, Durham DH1 3LE*
[7]*Department of Astronomy, Smith College, Northampton, MA 01063, USA*
[8]*Institute for Astronomy, University of Hawaii, Honolulu, HI 96822, USA*
[9]*Canada–France–Hawaii Telescope, Kamuela, HI 96743, USA*
[10]*Illinois Wesleyan University, P.O. Box 2900, Bloomington, IL 61702-2900, USA*

Accepted 2009 June 15. Received 2009 June 1; in original form 2009 March 24

ABSTRACT

We present results from a multiwavelength study of 29 sources (false detection probabilities <5 per cent) from a survey of the Great Observatories Origins Deep Survey-North (GOODS-N) field at 1.1 mm using the Astronomical Thermal Emission Camera (AzTEC). Comparing with existing 850 μm Submillimetre Common-User Bolometer Array (SCUBA) studies in the field, we examine differences in the source populations selected at the two wavelengths. The AzTEC observations uniformly cover the entire survey field to a 1σ depth of ∼1 mJy. Searching deep 1.4 GHz Very Large Array (VLA) and *Spitzer* 3–24 μm catalogues, we identify robust counterparts for 21 1.1 mm sources, and tentative associations for the remaining objects. The redshift distribution of AzTEC sources is inferred from available spectroscopic and photometric redshifts. We find a median redshift of $z = 2.7$, somewhat higher than $z = 2.0$ for 850 μm selected sources in the same field, and our lowest redshift identification lies at a spectroscopic redshift $z = 1.1460$. We measure the 850 μm to 1.1 mm colour of our sources and do not find evidence for '850 μm dropouts', which can be explained by the low signal-to-noise ratio of the observations. We also combine these observed colours with spectroscopic redshifts to derive the range of dust temperatures T, and dust emissivity indices β for the sample, concluding that existing estimates $T \sim 30$ K and $\beta \sim 1.75$ are consistent with these new data.

Key words: galaxies: formation – galaxies: high-redshift – galaxies: starburst – infrared: galaxies – submillimetre.

1 INTRODUCTION

Over the last decade observations at submillimetre (submm) and millimetre wavelengths (350–1200 μm) have been used to detect a population of luminous [$L_{\rm IR} = L(8\text{–}1000\ \mu\text{m}) > 10^{12}\ \rm L_\odot$] galaxies (e.g. Smail, Ivison & Blain 1997; Barger et al. 1998; Hughes et al. 1998; Eales et al. 1999; Cowie, Barger & Kneib 2002; Scott et al. 2002; Borys et al. 2003; Serjeant et al. 2003; Webb et al. 2003; Greve et al. 2004, 2008; Wang, Cowie & Barger 2004; Coppin et al. 2005; Laurent et al. 2005; Coppin et al. 2006; Knudsen et al. 2006; Bertoldi et al. 2007; Khan et al. 2007; Perera et al. 2008; Scott et al. 2008; Austermann et al. 2009; Devlin et al. 2009). These objects, referred to as submillimetre galaxies (SMGs), are thought to be high-redshift analogues of the local Ultra Luminous Infrared

★E-mail: echapin@phas.ubc.ca
†*Spitzer* Fellow.

Galaxy (ULIRG) population (Sanders & Mirabel 1996). Their large luminosities and apparent lack of significant active galactic nuclei (AGN) activity in most cases (e.g. Bautz et al. 2000; Hornschemeier et al. 2000; Almaini et al. 2003; Alexander et al. 2005; Pope et al. 2008) imply star-formation rates $\gtrsim$100–1000 $M_\odot$ yr^{-1}. With orders of magnitude larger space density at $z > 1$ than in the present-day Universe, it is presently believed that SMGs could represent an energetic early star-forming phase in the process that produces giant elliptical galaxies, and a significant fraction of the total star-formation rate density at $z \gtrsim 2$ (see Blain et al. 2002, for a review).

The identification of multiwavelength counterparts to SMGs is hindered by the angular resolution of the current generation of submm instruments (typically ∼10–20 arcsec), and the high surface density and faintness of counterparts in the optical/near-infrared (NIR), making unambiguous associations difficult. Significant progress has been made in the field by first searching for candidates in much lower surface density catalogues with higher astrometric precision, in particular using 1.4 GHz Very Large Array (VLA) interferometer maps, and deep 24 μm *Spitzer* observations. This method works with both radio and mid-IR data, wavelengths that, as in the submm, are biased towards the detection of star-forming galaxies: the radio synchrotron emission has a well-known correlation with the far-IR radiation that gets redshifted into the observed submm band, and 24 μm samples primarily thermal emission from warmer dust in the vicinity of star-forming regions. With the much improved positional uncertainties of ∼1 arcsec offered by these radio and mid-IR data sets, it is then possible to identify optical/NIR counterparts provided that they are bright enough (e.g. Ivison et al. 2002; Chapman et al. 2005; Pope et al. 2006; Ivison et al. 2007).

In this paper, we use this established procedure to identify counterparts to SMGs detected in a 1.1 mm map[1] of the Great Observatories Origins Deep Survey-North (GOODS-N; Perera et al. 2008) using the Astronomical Thermal Emission Camera (AzTEC, Wilson et al. 2008a). GOODS-N is one of several well-studied fields in the northern hemisphere that has the prerequisite radio data, as well as deep *Spitzer* coverage to identify counterparts. There is also an impressive collection of optical imaging [*Hubble Space Telescope* (*HST*) and ground-based], and optical spectroscopy for >1500 targets with which to study the detailed properties of individual objects once their positions are known.

Until recently, the most complete submm image towards GOODS-N was the Submillimetre Common-User Bolometer Array (SCUBA) 850 μm map of Borys et al. (2003) (see also Pope et al. 2005; Wall, Pope & Scott 2008) that was produced from a heterogeneous collection of data obtained by different groups with different observing modes (Hughes et al. 1998; Barger, Cowie & Richards 2000; Borys et al. 2002; Serjeant et al. 2003; Wang et al. 2004). This map produced a sample of nearly 40 sources, and was the subject of a detailed multiwavelength study (Borys et al. 2004; Pope et al. 2005, 2006). However, the spatially varying noise of the SCUBA map, combined with the desire to search for even higher redshift sources that are expected to be more easily detected at longer wavelengths due to the more favourable negative *K*-correction (e.g. Eales et al. 2003), motivated the survey of Perera et al. (2008) to uniformly map the entire area at 1.1 mm. The GOODS-N AzTEC map covers 245 arcmin^2 (matching the *Spitzer* coverage), has an 18 arcsec full-width half-maximum (FWHM) beam (compared with 15 arcsec for SCUBA at 850 μm) and reaches a uniform rms depth of 0.96–1.16 mJy beam^{-1}. Note that there is also a map covering a similar area made using Max-Planck Millimeter Bolometer Array (MAMBO) at 1.2 mm (Greve et al. 2008); those data have a smaller beam (11.1 arcsec FWHM), but slightly less uniform coverage with noise varying between 0.7 and 1.2 mJy beam^{-1}.

The 28 robust 1.1 mm sources identified in Perera et al. (2008) were detected with significances $>3.8\sigma$. In this paper, we present potential counterparts for all of these sources, as well as one new object that was obtained by deblending the brightest peak in the map, *AzGN* 1, revealing a faint source that we label *AzGN* 1.2 (corresponding to *GN* 20 and *GN* 20.2, respectively, in Pope et al. 2006 and Pope 2007). Note that the 1.1 mm *deboosted* flux densities given in this paper in Table A3 have been corrected for Eddington bias and in many cases have signal-to-noise ratios (S/N) $<3\sigma$: these values are the least biased estimates for the true flux densities, but do not reflect the robustness of the detections. The integrated negative tails of these distributions were used to estimate false detection probabilities, and a limit $p(S < 0) < 5$ per cent corresponds to the 3.8σ threshold mentioned above. Using extensive simulations, the actual spurious rate for the entire sample was estimated to be 1 or 2 sources in Perera et al. (2008).

We find robust counterparts for 21 objects, which we define to be objects with false-identification probabilities $P < 0.05$ within 6 arcsec. We also provide tentative identifications for the remaining sources, considering counterparts up to 10 arcsec away and $0.05 < P < 0.10$ (Section 2). These identifications enable us to report radio-IR spectral energy distributions (SEDs) using the VLA, SCUBA and *Spitzer* GOODS-N data. For the robust list, we identify spectroscopic redshifts for seven objects in the literature, and provide a combination of mid-IR and radio-(sub)mm photometric redshifts for the remaining 13 sources (Section 3). We compare our results with the existing SCUBA studies in this field to: (i) identify differences in the redshift distributions of sources selected at 850 μm and 1.1 mm; (ii) evaluate the effectiveness of searching for '850 μm dropouts' (objects detected at 1.1 mm but not at 850 μm) as a means for finding higher redshift SMGs; and (iii) probing the rest-frame distribution of dust properties of SMGs consistent with measurements in the two bands (Section 4).

2 COUNTERPART IDENTIFICATION

2.1 Radio and mid-IR matching catalogues

The radio and *Spitzer* catalogues that we use to find counterparts are generally the same as in Pope et al. (2006), and we refer the reader to that paper for further details. The only significant update to their analysis is an improved 1.4 GHz VLA radio map, with a 50 per cent reduction in the noise to ∼4–5 μJy rms across the AzTEC coverage region compared to that presented by Richards (2000), and about 25 per cent deeper than the map used by Pope et al. (2006). The complete data set contains a total of 165.5 h of VLA 1.4 GHz observations in A (128.5 h), B (28 h), C (7 h) and D (2 h) configuration. These data were combined, reduced and imaged using Astronomical Image Processing System (AIPS).[2] Full details of this analysis will be presented in Morrison et al. (in preparation). While the final product of that paper will be a 5σ catalogue, we have produced two deeper catalogues for use in this work: (i) an approximately 4σ catalogue with a surface density of 1.80 arcmin^{-2}, and (ii) a fainter 3σ radio catalogue with a surface

[1] Map available at http://www.astro.umass.edu/AzTEC/

[2] http://www.aips.nrao.edu/

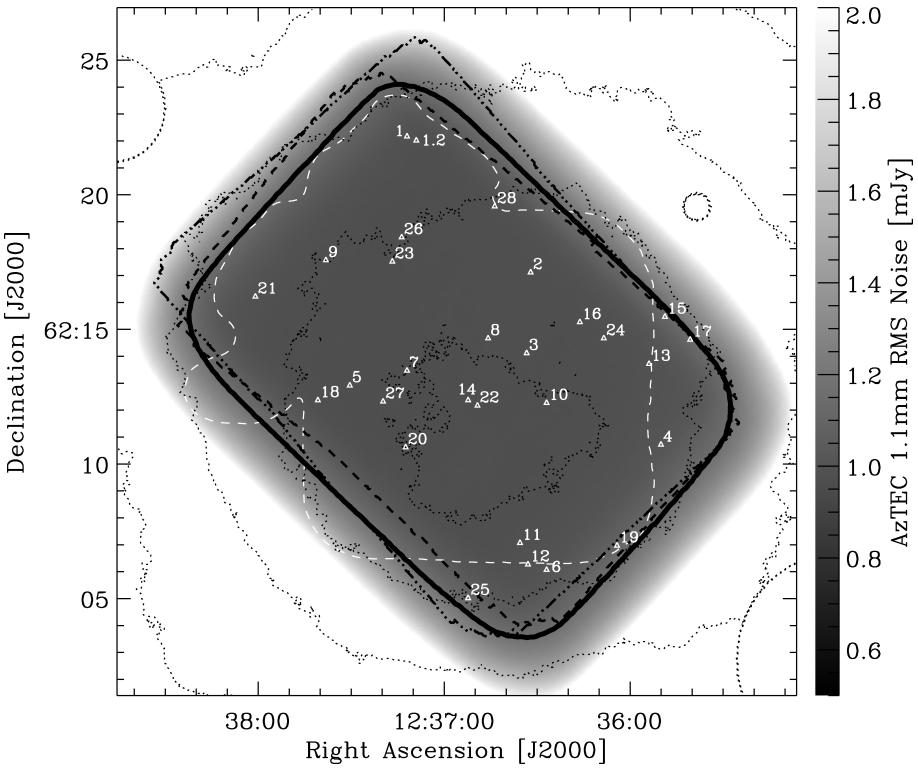

Figure 1. The relative coverage of data sets in GOODS-N used in this paper. The grey-scale indicates the rms noise in the AzTEC 1.1 mm map. The solid black contour corresponds to a noise of 1.16 mJy in this map, and is the region within which AzTEC sources (white numbered triangles) were extracted. The white dashed contour indicates the SCUBA 850 μm coverage with a noise less than 10 mJy. The black dashed contour shows the MIPS 24 μm coverage, and the dot–dashed lines the IRAC 3.6 μm coverage. Finally, the thin dotted contours indicate the surface density of VLA 1.4 GHz sources from the 4σ catalogue (0.5, 1.0, 1.5 and 2.0 arcmin^{-2}) measured in apertures with a radius of 0.1 deg. For reference, the half-power radius of the radio map noise is about 0.25 deg. The holes seen in these contours centred over 12:34:52 +62:03:41, 12:35:38 +62:19:32, and 12:38:48 +62:23:09 are regions of the map that were excised due to sidelobe structure caused by especially bright sources.

density of 3.52 arcmin^{-2} that initially contains a much larger fraction of spurious sources from which we select only objects that are coincident within 1 arcsec of 3σ detections in the 24 μm catalogue. In both cases, a radio catalogue of the given significance is constructed using the AIPS source extraction task SAD in signal-to-noise mode (using the uncorrected peak flux densities) which uses an rms map estimated from the task RMSD. After SAD detects the sources over a region encompassing the AzTEC data, it then fits Gaussian components to these sources, and in the process applies corrections for both the bandwidth smearing and primary beam attenuation. The final catalogues report these corrected flux densities, including any spatially resolved structure that increases the extent of the fitted Gaussians, without any additional 'by-hand' removal of problematic sources. The catalogues are, therefore, expected to contain a number of false positives, and begin to suffer incompleteness, at their respective flux density limits. The 3σ catalogue covers a slightly smaller area, as it is limited to the 24 μm coverage. For several AzTEC sources around the edge of the map, we therefore use only the 4σ radio catalogue to make identifications; see Fig. 1 for the relative coverage of each data set.

In Fig. 2, the integral source counts for the radio and mid-IR catalogues are shown. The horizontal axis has been extended to sufficiently faint flux densities to show the point at which each catalogue becomes incomplete (flat integral counts). Clearly the raw 3σ radio catalogue contains many spurious detections at $S_{1.4} \lesssim 25$ μJy, as the counts diverge steeply from the trend at brighter flux densities traced by both the 3σ and 4σ catalogues. However, the requirement of a 24 μm counterpart for each radio source drastically reduces the number of candidate detections in this flux density regime, effectively extending the faint counts to ∼15–20 μJy from the ∼20–25 μJy achieved in the 4σ catalogue. We note that while this technique enables us to extract fainter sources from the radio map (rejecting many of the spurious noise peaks), the requirement of 24 μm emission could lead to incompleteness [i.e. real radio sources that are not detected with Multiband Imaging Photometer for *Spitzer* (MIPS)], as the 24 μm channel samples rest-frame spectral features (e.g. polycyclic aromatic hydrocarbon emission and silicate absorption) that are not directly related to the radio emission. Nevertheless, it will be shown in the following sections that even with these potentially incomplete radio catalogues we identify a significant fraction of the 1.1 mm sources.

For simplicity, a fixed search radius was used to identify potential counterparts in the two catalogues, rather than a variable radius as a function of AzTEC S/N (see e.g. Ivison et al. 2007). There is also a relatively small dynamic range in AzTEC flux densities, and with fairly constant noise, so that most of the positional uncertainties would be similar in any case. Given a search radius and list of potential counterparts, the probability that a given candidate is a random association,'*P*', is calculated following the prescription of Downes et al. (1986), a method that is now used almost ubiquitously in the submm literature. This technique accounts for the surface density of sources in the matching catalogue as a function of brightness: if two potential identifications of different

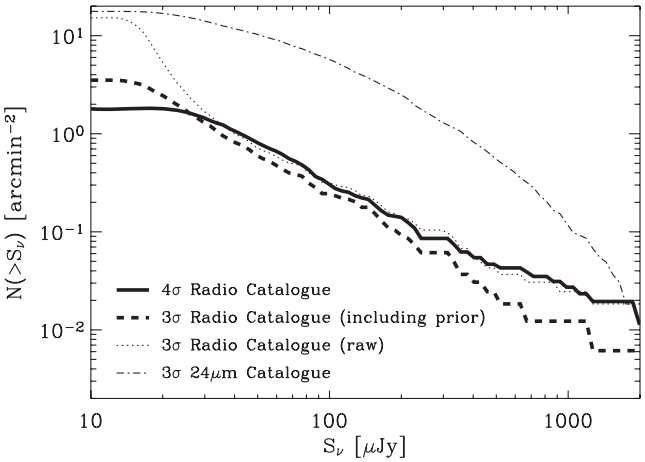

Figure 2. Integral source counts in the radio and mid-IR matching catalogues. The primary catalogue is the 4σ radio catalogue and its integral source counts within the solid black contour in Fig. 1 are shown by a solid line. A deeper 3σ radio catalogue was produced by the intersection of a raw 3σ radio catalogue with the 3σ 24 μm catalogue. The counts from the two raw source catalogues are shown by the dotted and dot–dashed lines, respectively, measured within the area common to the solid black and black dashed contours in Fig. 1. While the raw 3σ radio catalogue has a huge increase of sources at $S_{1.4} < 25$ μJy, indicating many spurious detections, the requirement of a 24 μm counterpart rejects many of these sources, such that the remaining counts at fainter flux densities follow the trend established at the bright end, but extending to a fainter limit than the 4σ catalogue.

brightnesses lie at the same distance from the AzTEC source, the rarer brighter object will be assigned a lower value of P. We have used the raw measured integral source counts in the matching catalogues (Fig. 2) for this calculation, rather than a model. Since the radio catalogues undoubtedly contain a number of spurious sources near the detection thresholds, this procedure will naturally account for them by down-weighting the robustness of proposed faint identifications where the surface density is much greater.

We also investigated the use of spatially varying measurements of the counts. Since the noise depth of the radio map falls off towards the edge of the AzTEC coverage, so do the counts in the radio catalogues. We chose an aperture with radius 0.1° (significantly smaller than the ∼ 0.25° half-power radius of the VLA map noise) in which we measured the integral radio counts centred over each position. For the 4σ radio catalogue, this resulted in a variation of the total surface density ranging from about 2.4 arcmin^{-2} at the centre of the map to 1.0–1.5 arcmin^{-2} along the edges (Fig. 1). We experimented with measurements of P using these modified counts at the locations of each AzTEC source. With the increased source density towards the centre of the map, values of P are increased slightly, and conversely values of P are decreased slightly towards the edges. However, the changes in individual values of P are generally <20 per cent, and the only effects of using this calculation on the final list of robust identifications would be to add *AzGN* 2, as P would drop to 0.050 from 0.051 for the single radio source within 6 arcsec, and similarly, the second radio source near *AzGN* 18 would be added, with P dropping to 0.047 from 0.051 (this object was already identified as a radio double, *GN* 38, in Pope et al. 2006, and the photometric redshift estimates are consistent with them being at the same distance). Since the differences are small, and the simpler calculation gives a slightly more conservative list of potential counterparts, we elected to use only the radio and mid-IR number counts averaged across the entire region of AzTEC coverage presented in Fig. 2. Average source counts were also used by Pope et al. (2006) and Greve et al. (2008) in their calculations of P to find SMG counterparts in this field.

2.2 Choice of search radius

A search radius was chosen to provide a reasonable level of completeness, while minimizing the number of false identifications. In Fig. 3, we plot the fraction of AzTEC sources with at least one such counterpart in the 4σ radio catalogue as a function of search radius with $P < 0.05$ (solid black line). The function initially rises as most true counterparts are eventually detected, reaches a peak of 62 per cent at 6–7 arcsec, and then drops as potential identifications again become improbable due to the increasing chance of a spurious detection with such a large search radius. In contrast, if all radio sources within the search radius are considered, the total fraction with potential counterparts continues to grow (solid grey line). To demonstrate the effectiveness of cuts on P to lower the false identification rate, we repeat these calculations using random positions. Using the cut on P (dashed black line) results in a plateau at the expected fraction of ∼0.05, coincidentally, also at a search radius of 6 arcsec. Without the cut, the spurious identification fraction (grey dashed line) continues to rise to ∼100 per cent by a radius of 60 arcsec.

The chosen search radius of 6 arcsec is smaller than those used for SCUBA sources, typically in the range of 7–8 arcsec for objects with similar S/N (e.g. Ivison et al. 2002; Webb et al. 2003; Borys et al. 2004; Pope et al. 2006; Ivison et al. 2007), despite AzTEC having a slightly larger beam. Borys et al. (2004) used a different method to estimate a search radius for counterparts to SCUBA sources in GOODS-N, finding a value of 7 arcsec to be appropriate. We repeated their analysis with our data, however, and concluded again that we should use 6 arcsec. This test sug-

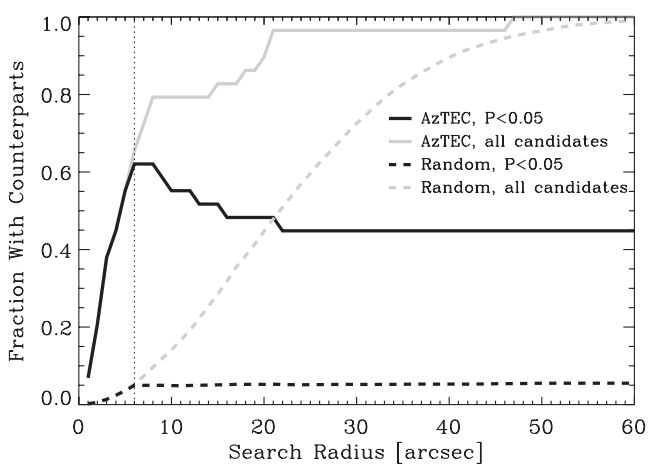

Figure 3. The fraction of AzTEC sources with robust 4σ 1.4 GHz ($P <$ 0.05) candidate identifications as a function of search radius (solid black line) compared with the fraction of sources with any candidate identifications (no cut on P, solid grey line). For reference, the black and grey dashed lines indicate the spurious counterpart detection rates using random positions with and without the $P < 0.05$ cut, respectively. A search radius of 6 arcsec (vertical dotted line) is used since it gives the peak robust identification fraction. It also happens to be where the random fraction corresponds to 5 per cent. We chose this 6 arcsec radius to search for all candidates, even in the 3σ radio catalogue. In the event that no robust counterparts with $P <$ 0.05 can be identified within 6 arcsec, the search radius is extended out to 10 arcsec to find tentative identifications.

gests that the smaller resulting search radius is a property of the data, rather than the method we used to calculate it. As a further consistency check, recent Submillimeter Array (SMA) follow-up of AzTEC sources detected in other fields using the same pointing model as that employed here has shown excellent agreement. For example, Younger et al. (2007) found positional uncertainties <4 arcsec between SMA and AzTEC centroids of millimetre sources in the Cosmological Evolution Survey (COSMOS) field detected with generally higher S/N than the objects discussed in this paper.

Finally, we note in Fig. 3 that the fraction of AzTEC sources with *any* 4σ radio candidates beyond 6 arcsec (no cut on P, grey solid line) continues to grow significantly faster (from ∼65 to 80 per cent) than the spurious rate (grey dashed line, from ∼5 to 10 per cent) to a search radius of 8 arcsec. This suggests that ∼70 per cent of the entire AzTEC sample has counterparts in the 4σ radio catalogue, of which 10 per cent, about three objects, are within 6–8 arcsec of the AzTEC centroids. There is a radio source within 47 arcsec of every AzTEC centroid, although the additional objects encountered beyond ∼10 arcsec are almost certainly chance alignments.

2.3 Radio and mid-IR identifications

We first search for counterparts in the 4σ radio catalogue with $P < 0.05$, and if none are found within 6 arcsec, we proceed to search in the 3σ catalogue using the same radius and cut on P. This procedure gives us a robust sample that will subsequently be analysed in detail. In cases where no such counterparts can be found, we relax the search to identify more tentative counterparts out to a radius of 10 arcsec, and/or $P < 0.10$. Since these search parameters are expected to result in a much higher fraction of chance alignments, this extended catalogue is not used to measure properties of the general 1.1 mm galaxy population, and is simply included for completeness (although statistically speaking most of these tentative identifications are probably correct). In one case (*AzGN* 27), neither radio catalogue yields a source within 6 arcsec nor are there any counterparts with $P < 0.05$ out to 10 arcsec, so we search in the MIPS 24 μm catalogue (using the counts in Fig. 2 to calculate P), finding two potential identifications (however, we are still able to estimate radio flux densities by performing photometry in the VLA map at the MIPS positions). While possibly containing the correct counterparts for this particular object, the 24 μm catalogue is not, in general, as useful as the radio catalogues, due to a significantly greater surface density and hence chance of identifying random interlopers (see also Ivison et al. 2007).

In total, this procedure yields at least one counterpart within 6 arcsec for 26/29 AzTEC sources, 22 of which are robust with $P < 0.05$. Of the robust identifications, 18 were found in the 4σ radio catalogue, three in the 3σ radio catalogue and one in the MIPS 24 μm catalogue. Of the tentative associations within 6 arcsec, one was identified in the 4σ radio catalogue and three in the 3σ radio catalogue. Finally, all of the remaining 3/29 AzTEC sources have at least one tentative counterpart in the range $6 < r < 10$ arcsec in the 4σ radio catalogue. These results are summarized in Fig. 4 and Table A2. The SEDs for the proposed counterparts are given in Table A3. Additional notes for each source can be found in Appendix B.

2.4 False identification rate

We can estimate the number of spurious identifications for the 26 potential counterparts found within 6 arcsec by summing their P values, which gives 0.85. This implies that of those 26 AzTEC sources, about one of the identifications within 6 arcsec is expected to be spurious (noting that several sources have multiple proposed identifications). To understand how to interpret this result in terms of overall completeness, we consider several factors. First, the AzTEC source list is expected to have ∼1–2 spurious detections (Perera et al. 2008). Secondly, due to positional uncertainties, some of the true counterparts will lie beyond 6 arcsec. We adopt the radial offset distribution of Ivison et al. (2007), $r\ \exp(-r^2/2\sigma^2)$, with $\sigma \sim 0.6 \times \mathrm{FWHM/S/N}$, which assumes a symmetric Gaussian beam and uncorrelated map noise. The cumulative distribution of this analytic probability density function (PDF) results in a shape very similar to the numerical simulations of Scott et al. (2008) for AzTEC sources in the COSMOS field. Taking FWHM = 18 arcsec, and the S/N for raw map flux densities (before deboosting), we would only expect to encounter counterparts within 6 arcsec for 27.5/29 sources on average if they were all real (neglecting positional uncertainties in the matching catalogue). However, we would confidently expect to find *all* of the objects within 10 arcsec. Since we do not know which (if any) of the AzTEC sources are false positives, we simply apply this fraction to the expected number of real sources calculated above, and find that there should be ∼26–27 real sources with true positions within 6 arcsec of their 1.1 mm centroids. This expectation is consistent with our identification rate within 6 arcsec of ∼25–26 out of 29 sources, although we stress that this statistical argument does not necessarily imply that the unmatched sources are spurious. We find P values less than 0.05 for only 21 of the sources encountered within 6 arcsec (excluding *AzGN* 14 as noted below). While it may be the case that most of the remaining five sources are in fact associated with the 1.1 mm objects, it is also possible that the true counterparts are simply fainter in the radio than the catalogue limit. We cannot distinguish between these two cases in the present study given the positional uncertainties in the AzTEC centroids.

As a final warning, as with all studies that use P to evaluate chance alignment probabilities, there is an underlying assumption that the matching catalogues are spatially unclustered. Two examples of ways in which this condition could be broken are increased surface density of sources in the vicinity of SMGs due to multiple catalogue entries being associated with the same physical structure (such as a galaxy cluster), or foreground lensing of background objects (an effect which is in fact commonly used to identify faint SMGs, e.g. Smail et al. 2002). In both of these cases, P would be biased low. We do not attempt to correct for these effects in this work, but we alert the reader that the evidence for such cases in GOODS-N will be discussed in the following sections: the particularly complicated identification of a counterpart for *AzGN* 14 (also known *HDF* 850.1, Hughes et al. 1998) which caused us to drop it from the analysis in this paper; and the potential presence of a protocluster at redshift $z \sim 4$.

2.5 Comparison with SCUBA identifications

Since 12 of the 29 objects discussed in this paper were also detected by SCUBA (see Table A2) and identified in the radio and mid-IR using similar techniques (Pope et al. 2006; Wall et al. 2008), it is useful to compare proposed identifications to see how the new AzTEC positions and deeper radio catalogues affect the results. We exclude *AzGN* 14/*GN* 14 (*HDF* 850.1) from this comparison (and most of the remaining analysis in this paper) as its true counterpart has been under debate for some time due to the suspected obscuration by a foreground elliptical (see Dunlop et al. 2004; Cowie et al. 2009, and notes in Appendix B). Of the remaining 11 overlapping sources, we propose identical counterparts for eight of those

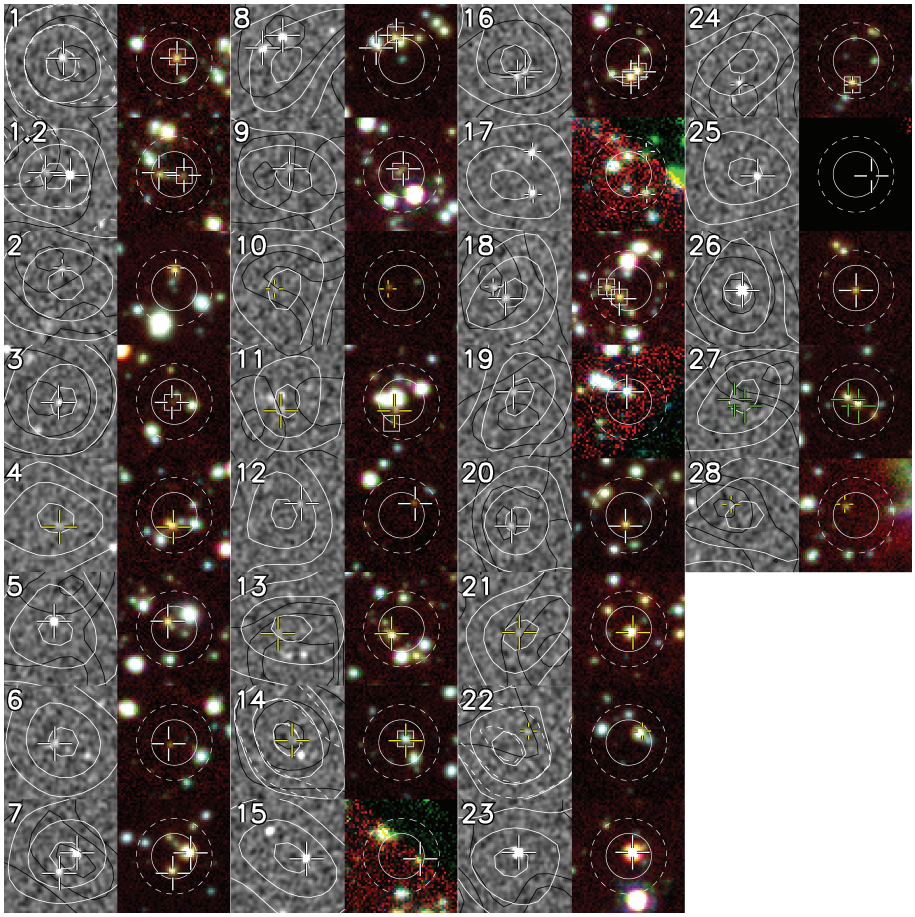

Figure 4. 30 × 30 arcsec^2 postage stamps showing AzTEC counterpart identifications in GOODS-N. The left-hand panels show the VLA 1.4 GHz map stretched between −20 μJy (black) and +30 μJy (white). The contours indicate fractions 0.1, 0.5 and 0.9 of the peak S/N in the AzTEC (white) and SCUBA (black; not always available) postage stamps. In addition, *AzGN* 1, *AzGN* 1.2, *AzGN* 14 and *AzGN* 22 have had the effects of nearby blended sources removed. The undeblended AzTEC map contours are shown with dashed white lines for comparison. Cross-hairs indicate the locations of potential counterparts from the catalogues in which they were originally identified: white for the 4σ radio catalogue; yellow for the 3σ radio catalogue; and green for the MIPS 24 μm catalogue. Long cross-hairs correspond to IDs with $P \leq 0.05$ and small cross-hairs for $P > 0.05$. The right-hand panels are false-colour images constructed from IRAC 3.6 (blue), 4.5 (green) and 5.8 μm (red) exposures. Squares indicate the locations of radio/IR counterparts to SCUBA sources proposed in Pope et al. (2006). The solid and dashed circles indicate search radii of 6 and 10 arcsec, respectively. Approximately 1 or 2 of the AzTEC sources are expected to be false positives.

objects. For *AzGN* 1.2, we find that both the proposed counterpart of Pope et al. (2006) ($P = 0.005$ in this paper) and a second fainter radio object (with $P = 0.037$, also noted by Daddi et al. 2009a) are both robust identifications by our definition. In another similar case, only one object from a radio double identified by Pope et al. (2006) for *AzGN* 18 is strictly a robust counterpart ($P = 0.032$ in this paper), while the second radio source misses the cut, with $P = 0.051$. The only object for which we propose a completely different counterpart is *AzGN* 11/*GN* 27, which was classified as 'tentative' in the SCUBA map: the Advanced Camera for Surveys (ACS)/Infrared Array Camera (IRAC) identification from Pope et al. (2006) is absent in the 1.4 GHz map, and we instead propose a radio source that lies slightly to the north, with $P = 0.027$.

3 REDSHIFT DISTRIBUTION

Some recent surveys at 1.1–1.2 mm claim to detect higher redshifts than SCUBA surveys at 850 μm (e.g. Younger et al. 2007; Greve et al. 2008), while others find redshift distributions that are indistinguishable, possibly due to small sample sizes (e.g. Greve et al. 2004; Bertoldi et al. 2007). For this AzTEC survey, we more accurately quantify any differences using greatly improved redshift information, and comparing directly to the SCUBA results in this field using the same methodology. While the uncertainty in the 1.1 mm distribution derived from our data is large, due to the relatively small sample size, and cosmic variance resulting from the area of GOODS-N, this differential measurement yields a useful comparison between the two bands.

A number of groups have obtained spectroscopic redshifts in GOODS-N (e.g. Cohen et al. 2000; Cowie et al. 2004; Wirth et al. 2004; Chapman et al. 2005; Reddy et al. 2006; Barger, Cowie & Wang 2008; Daddi et al. 2009a; Pope et al. 2008; Daddi et al. 2009b, Stern et al., in preparation). We found spectroscopic redshifts for 10 of our proposed AzTEC counterparts in these publicly available data sets (see Table A2). However, one of those redshifts (*AzGN* 8) corresponds to the least favourable counterpart within the search radius (see the discussion for this source in Appendix B). Another similar case is *AzGN* 27 for which a spectroscopic redshift has been obtained only for the more distant of two potential counterparts. Finally, two radio sources that appear to be associated with the single object *AzGN* 7 lie at redshifts $z = 1.996$ and 1.992, and we assign a single redshift of $z = 1.994$,

which is sufficiently precise for the purposes of this paper. Therefore, our sample of 21 sources with unambiguous identifications contains only 7/21 sources with spectroscopic redshifts. This fraction is considerably lower than the 15/20 spectroscopic redshifts for robust counterparts from the Pope et al. (2006) SCUBA sample (also excluding *HDF* 850.1), including the two new redshifts for *GN* 20 and *GN* 20.2 from Daddi et al. (2009a), the redshift for *GN* 10 from Daddi et al. (2009b) and two additional *Spitzer* Infrared Spectrograph (IRS) redshifts from Pope et al. (2008). However, we are not surprised at this lower rate since we rely on archival data for the redshifts of counterparts to new AzTEC sources, whereas many of the spectroscopic redshifts for SCUBA sources were obtained using targeted follow-up of proposed identifications.

For sources without a spectroscopic redshift, we first searched for optical photometric redshift estimates. As none were found, we instead employed two photometric redshift calculations using longer wavelength data. The first, $z_{\rm ir}$, is a simple function of the *Spitzer* photometry with coefficients derived from fits to SCUBA sources in GOODS-N with spectroscopic redshifts (Pope et al. 2006). Although this method does not assume any particular SED, it benefits from the 1.6 μm stellar bump that produces a strong characteristic feature in the observed IRAC 3.6–8.0 μm bands for sources at redshifts $1 \lesssim z \lesssim 4$ (Simpson & Eisenhardt 1999; Sawicki 2002). Such an empirical calculation may provide less biased results than fitting spectral templates to the data since there are degeneracies between the derived redshift and assumptions about the starburst producing the stellar bump (see discussion in Yun et al. 2008). While the residuals for this functional fit are relatively small (with a maximum $\Delta z = 0.4$), no uncertainties are provided in Pope et al. (2006) for the remaining sources. However, a similar photometric redshift estimator was derived by Wilson et al. (2008b), and a comparison with spectroscopic redshifts for SMGs from several fields [including SCUBA sources from both GOODS-N and SCUBA Half Degree Extragalatic Survey (SHADES)] finds that a 1σ error envelope $\Delta z = 0.15(1 + z)$ is a reasonable uncertainty estimate for 15 SMGs at redshifts $0 \lesssim z \lesssim 3$. We have compared the Pope et al. (2006) and Wilson et al. (2008b) photometric redshift formulae for our data and find that of the seven robust identifications with spectroscopic redshifts both methods provide estimates consistent with the spectroscopic measurements for the three sources at $z < 3$, within the Wilson et al. (2008b) error envelope. However, both estimates are biased low at $z > 3$, more so using the Wilson et al. (2008b) redshift estimator. We also checked the scatter between the two methods for all of the robust identifications finding that they both gave answers compatible with the Wilson et al. (2008b) uncertainty estimate. This bias and scatter are unsurprising as both formulae were fit to SMGs with spectroscopic redshifts $z \lesssim 3$. In this work, we assume the 1σ uncertainties are also $\Delta z_{\rm ir} = 0.15(1 + z)$, but warn the reader that the redshifts of more distant objects are probably systematically underestimated with this technique.

The second photometric redshift indicator, $z_{\rm rm}$, uses the radio and (sub)mm flux densities fit to templates of local galaxies assuming the radio-IR correlation holds at high redshift (e.g. Carilli & Yun 1999; Aretxaga et al. 2007). This method provides the only redshift estimates for a handful of sources around the edges of the AzTEC map where there is no *Spitzer* or optical coverage from the GOODS survey (the entire AzTEC survey area overlaps with the 1.4 GHz data). Our redshifts are calculated using the same methodology as Aretxaga et al. (2007) and summarized in Table A2. We note that the quoted 68 per cent confidence intervals are theoretical estimations; Aretxaga et al. (2007) checked the scatter between photometric and spectroscopic redshifts for a sample of SMGs with radio and submm data of similar quality to GOODS-N finding an empirical symmetric 1σ scatter of $\Delta z_{\rm rm} = 0.8$. We also adopt this uncertainty for consistency with the empirically measured uncertainties for $z_{\rm ir}$.

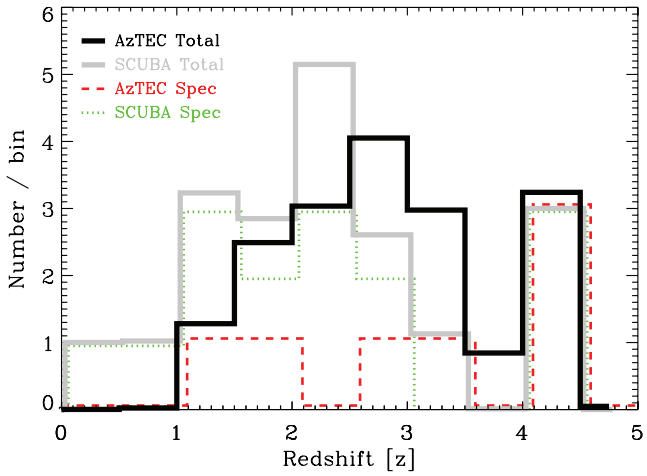

Figure 5. The redshift distribution of the 18 robustly identified 1.1 mm sources in GOODS-N (black histogram) with redshifts, adopting unique identifications from Table A2 with the smallest P values for each source. The grey histogram is the redshift distribution of 20 similarly robust SCUBA 850 μm sources from Pope et al. (2006), excluding *GN* 14, and updating some spectroscopic redshifts based on Daddi et al. (2009a,b) and Pope et al. (2008). There is not an integral number of sources in each bin because the uncertainties in photometric redshifts have been included. The results of K–S and M–W tests indicate chance probabilities $p_{\rm KS} = 0.05$ and $p_{\rm MW} = 0.01$, that both histograms were drawn from the same parent distribution (although they can be larger when individual redshift uncertainties are included, see Section 3). For comparison, the dashed red and green dotted histograms show the distribution of spectroscopic redshifts for AzTEC and SCUBA sources, respectively. The excess number of objects in the $4.0 < z < 4.5$ bin may be members of a high-redshift protocluster (Daddi et al. 2009a,b).

In Fig. 5, we show the AzTEC redshift distribution of the 18/21 robust ($P < 0.05$) identifications (black line) for which there are redshifts (spectroscopic or photometric). The remaining three objects (*AzGN* 15, *AzGN* 19 and *AzGN* 25) have only lower limits on their redshifts, and have been excluded from the histogram and subsequent analysis. For the objects lacking spectroscopic redshifts, we use the photometric redshift estimates, including their uncertainty distributions to divide them amongst several bins if necessary. When both $z_{\rm ir}$ and $z_{\rm rm}$ are available, we calculate the variance-weighted mean redshifts. We feel we are justified in doing this because the two estimators depend on data and spectral features at completely different wavelengths, and are therefore independent of each other. We then calculate the distribution for 20 similarly robust 850 μm sources (grey line) from Pope et al. (2006) in the same way for comparison. Note that, as in this work, we have excluded *HDF* 850.1 (*GN* 14/*AzGN* 14) from their redshift distribution. In addition, we have updated redshifts for several sources using new spectroscopic data (Daddi et al. 2009a,b; Pope et al. 2008).

The median redshift of the AzTEC sample is $z = 2.7$, with an interquartile range of 2.1–3.4. In contrast, the median of the SCUBA sample shown here is $z = 2.0$ with an interquartile range 1.3–2.6. For reference, the 14 SCUBA sources with spectroscopic redshifts (green dotted histogram in Fig. 5) has a median $z = 2.0$ and the 7 AzTEC sources (red dashed histogram) $z = 3.19$, both in good agreement with the full distributions despite the small number of

objects. It is also worth noting that the spike of spectroscopic redshifts in the $4.0 < z < 4.5$ bin seen at both wavelengths was found via targeted follow-up to SCUBA sources by Daddi et al. (2009a) and Daddi et al. (2009b) that are thought to be members of a proposed protocluster at $z \sim 4$. Although not included in the distribution, a recent study by Cowie et al. (2009) suggests that *HDF* 850.1 may also be a member of this high-redshift structure.

We note that while the AzTEC sample appears to lie at slightly higher redshift than the SCUBA sample, we have had to rely more heavily on highly uncertain photometric estimates than in Pope et al. (2006). However, the bias is likely to be towards lower rather than higher redshifts due to the nature of $z_{\rm ir}$.

Next, taking the SCUBA and AzTEC redshift distributions at face value (including photometric redshifts), we have used the Kolmogorov–Smirnov (K–S) and Mann–Whitney *U* (M–W) non-parametric tests for assessing how different they are. These tests are fair since both samples were drawn from the same region of space, and no extra uncertainty needs to be included to account for cosmic variance. Both methods operate on discrete samples so we first assign the mean redshift to each object from its uncertainty distribution. The K–S test, which is sensitive to more general differences in the distributions (both the central values and tails), gives a chance probability $p_{\rm KS} = 0.05$ that both samples were drawn from the same parent redshift distribution. The M–W test, which is mostly sensitive to differences in the central values of the distributions, gives a smaller chance probability $p_{\rm MW} = 0.01$. However, we note that the uncertainties for objects with photometric redshifts can be as large as $\Delta z \sim 0.8$, comparable to the width of the entire population. To evaluate the spread in K–S and M–W probabilities that are consistent with our sample, we generate 10 000 mock samples at each wavelength drawing individual redshifts at random from the uncertainty distributions for each object. We find that 68 per cent of the time, we obtain values $p_{\rm KS} < 0.15$ and $p_{\rm MW} < 0.04$. These tests show that, even with large individual uncertainties, the shift to higher redshifts at 1.1 mm compared to 850 μm appears to be statistically significant.

The SCUBA sample consists of a broader dynamic range in flux density than the AzTEC sample, due to the varying map depths, and the fact that different redshift populations may be present in the deep and shallow regions of the map (Pope et al. 2006; Wall et al. 2008). It, therefore, may be the case that at least some of the differences between these distributions are a result of a depth rather than wavelength selection effect.

One potential concern with this comparison is that, due to a bias to higher redshifts at fainter flux densities (e.g. Chapman et al. 2005), the deeper radio catalogues used for matching in this survey simply detect more distant potential counterparts than in Pope et al. (2006). We checked the distribution of radio brightness with redshift for our sample and found that the six faintest proposed radio counterparts lie in the redshift interval $2 < z < 3$. Removing them, while broadening the remaining redshift distribution slightly, does not shift the median appreciably. However, if we remove sources with even brighter radio flux densities, we in fact begin to bias the sample to *higher* redshifts. Combined with the fact that we find most of the same counterparts for sources that appear in both the AzTEC and SCUBA surveys (Section 2.5), we conclude that the intrinsic rest-frame scatter of radio luminosities in SMGs dominates any differences in the radio properties of 850 μm and 1.1 mm selected samples.

The *lowest* redshift that we find is *AzGN* 23 at $z = 1.146$. This demonstrates the ability of mm-wavelength surveys to effectively select galaxies at $z > 1$, with little contamination from nearby objects. Assuming that our identification procedure and redshift estimates are correct, and given the completeness of our survey, there is therefore little room for a significant tail to extremely high redshifts. Since the negative *K*-correction at 1.1 mm could in principle enable us to detect SMGs easily out to a redshift $z \sim 10$ (Blain et al. 2002), the fact that objects at $z \gtrsim 4.5$ do not appear in our sample demonstrates that they do not exist in large quantities, and would therefore require much larger surveys to find them. Only if many of the identifications for these AzTEC sources are in fact more complicated (as in the case of *HDF* 850.1) may the door still be open for a significant fraction of the SMG population to lie at generally higher redshifts ($z > 4.5$).

4 SPECTRAL ENERGY DISTRIBUTIONS

With redshift estimates in hand, we are now in a position to probe the rest-frame SEDs of our sample. Although we have photometry at a number of wavelengths spanning 3.6 μm to 20 cm for most of the objects, the most interesting new constraints that we place on these SEDs is the shape of their rest-frame far-IR emission that peaks near 100 μm in the rest frame, produced by thermal dust grain emission. This emission accounts for most of the bolometric luminosity in SMGs, and it is generally believed to be produced by optically obscured star formation in most cases (e.g. Blain et al. 2002), much like locally observed ULIRGs. The far-IR luminosity is, therefore, crucial for estimating star-formation rates. The far-IR SED also provides a direct probe of the total dust mass in a galaxy. However, both the bolometric luminosity and dust mass are critically dependent on the dust temperature, T, and the dust grain emissivity, β (Hildebrand 1983). Due to a dearth of data at the necessary wavelengths, spanning ∼100–1000 μm, most authors either attempt to fit a simple three-parameter modified blackbody spectrum for a population of dust grains at a single temperature, $S_\nu = A\nu^\beta B_\nu(T)$ (where A is the amplitude), or adopt a single SED and normalize it to the (sub)mm data point. Since only a single (sub)mm data point is usually available, this latter compromise is often made. A census of recent studies finds broad agreement that the most typical values are $T_{\rm d} = 30$–35 K for SMGs, with an allowed range that is somewhat broader than this (Chapman et al. 2005; Kovács et al. 2006; Pope et al. 2006; Huynh et al. 2007; Coppin et al. 2008). However, the estimates of $T_{\rm d}$ and β are highly correlated, because of the limited range of wavelengths for which data exist.

In GOODS-N, the combination of 1.1 mm and 850 μm flux densities sample wavelengths longward of the rest-frame far-IR peak. The ratio $S_{850}/S_{1.1}$ defines a family of two-parameter SEDs (T and β) for each source which we will use to check for consistency with previous measurements of the thermal SEDs of SMGs at typically shorter wavelengths.

4.1 Correcting for flux density bias

We first estimate unbiased 1.1 mm and 850 μm flux densities for the AzTEC sources. As discussed in Perera et al. (2008), the 1.1 mm flux densities are biased high because they are selected from a low S/N list of peaks coming from a counts distribution that falls steeply with increasing brightness. The correction for this bias followed the prescription of Coppin et al. (2005), and we adopt those posterior flux density distributions here. While this correction does not account for the additional effect of source blending, the AzTEC GOODS-N survey is shallower than the estimated confusion limit, and the sources that appear to be confused have been fit explicitly in this paper using two components. Rather than cross-matching

the AzTEC catalogue with the SCUBA catalogue to obtain 850 μm flux densities, which itself suffers flux density bias (and since the SCUBA data are also too shallow in some areas to provide flux densities for many of our sources), we instead directly measure the 850 μm map at the positions of proposed counterparts. Provided that these counterparts are correct, and 850 μm source confusion is negligible, this photometry yields unbiased 850 μm flux densities with symmetric Gaussian uncertainties for *all* 24/29 AzTEC sources that land within the region of SCUBA coverage. However, due to the wide range in sensitivities only nine objects have 850 μm detections with a significance of at least 3σ.

4.2 Searching for '850 μm dropouts'

It has been suggested that in regions where observations at both 850 μm and ∼1.1 mm exist '850 μm dropouts', i.e. sources that are detected by AzTEC but not by SCUBA, can be used to select predominantly higher redshift sources (Greve et al. 2004, 2008). This technique is expected to work for the same reason that the AzTEC redshift distribution is slightly higher than the SCUBA sample: there is an increased submm negative K-correction at 1.1 mm compared to 850 μm (i.e. the ratio of 850 μm to 1.2 mm flux density, $S_{850}/S_{1.2}$, decreases with redshift, seen for example in Fig. 4 of Eales et al. 2003). In this study, we proceed by first testing the hypothesis of a single intrinsic observed flux density ratio $R \equiv S_{850}/S_{1.1}$, by measuring R for several high-S/N objects selected in the AzTEC map, and then searching for dropouts in the SCUBA map relative to this average colour. We also repeat this analysis in the opposite direction (for completeness), searching for SCUBA sources that are dropouts in the AzTEC map.

We measure R using sources with deboosted flux densities that have significances $>3\sigma$ in both bands: *AzGN* 1, *AzGN* 3, *AzGN* 7 and *AzGN* 8, giving similar values 1.72, 1.96, 1.67 and 2.04, respectively. We adopt the mean $R = 1.8$. For reference, thermal emission from a galaxy with $T = 30$ K and $\beta = 1.5$ at $z = 2.5$ would give an observed ratio 1.85. In order to compare our measurement with values reported for SCUBA (850 μm) and MAMBO (1.2 mm) overlap, we use the same model SED to estimate how much larger the $S_{850}/S_{1.2}$ ratio would be, finding that the scaled result is 2.3, near the centre of the distributions reported by Greve et al. (2004, 2008). Similarly, we scale our result to estimate the ratio $S_{890}/S_{1.1}$ for 890 μm SMA follow-up of AzTEC sources, finding a ratio of 1.6. This value is consistent with 1.4 ± 0.3 reported by Younger et al. (2007).

Next we use our measured R to scale the deboosted 1.1 mm flux density distributions for the entire sample to 850 μm. For simplicity, we approximate the scaled 850 μm predicted flux density distributions as Gaussians with mean values $s_{\rm m}$ given by the modes, and standard deviations $\sigma_{\rm m}$ as half of the 68 per cent confidence intervals. If our hypothesis of a single observed ratio were true, given the observed 850 μm data with mean flux densities $s_{\rm d}$ and standard deviations $\sigma_{\rm d}$, we would expect the residuals $(s_{\rm m} - s_{\rm d})/\sqrt{\sigma_{\rm m}^2 + \sigma_{\rm d}^2}$ to be normally distributed with mean 0 and standard deviation 1. For the 20 objects that do not have 3σ detections at 850 μm, we calculate the sample mean and standard deviation of the residuals, giving -0.1 ± 1.4. This calculation confirms that a ratio of 1.8 is a good estimate for the central value of the observed distribution $S_{850}/S_{1.1}$ (left-hand panel of Fig. 6).

Since the residual is broader than expected (by a factor $\sim\sqrt{2}$), we conclude that the *intrinsic* spread in R produces uncertainties of the same order as our measurement errors. Note that the spread in R for a $T = 30\,K$, $\beta = 1.5$ SED from redshifts $z = 1$–4 is only 2.1–1.6, so that part of the measured spread must be due to a range of rest-frame dust emission spectra in addition to the redshift distribution. We note

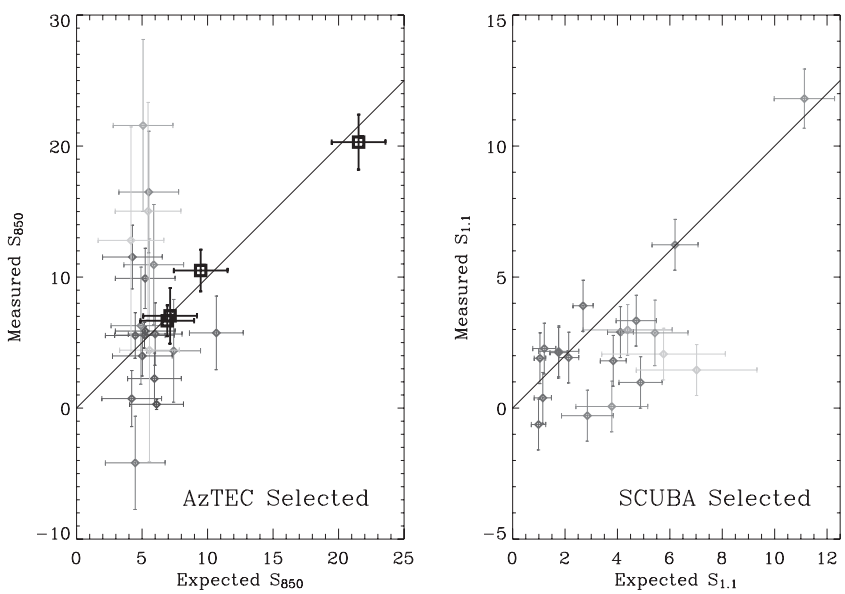

Figure 6. Measured flux densities (vertical axes) compared with predicted flux densities (horizontal axes) for AzTEC (1.1 mm) and SCUBA (850 μm) selected source lists. Left-hand panel: measured SCUBA flux densities at the locations of counterparts proposed for AzTEC sources. The predicted SCUBA flux densities were scaled from the deboosted AzTEC measurements using the ratio of $S_{850}/S_{1.1}$ fit to the four most significant simultaneous detections in both the AzTEC and SCUBA maps (thick square symbols), yielding 1.8. We also plot the relation for the remaining 20 objects measured in both bands (diamonds). The symbols and error bars are coloured more lightly if they are less significant (combined observed and predicted 850 μm uncertainties). This plot shows symmetric scatter about the single-colour relation, and hence no clear evidence for 850 μm dropouts that would fall systematically below the line. Right-hand panel: AzTEC flux densities at the locations of counterparts to SCUBA sources. The predicted values are derived from the deboosted SCUBA flux densities reported in Pope et al. (2006) by dividing them by the same factor of 1.8. The low outliers are primarily low-S/N SCUBA measurements (larger horizontal error bars) suggesting that they have been insufficiently deboosted.

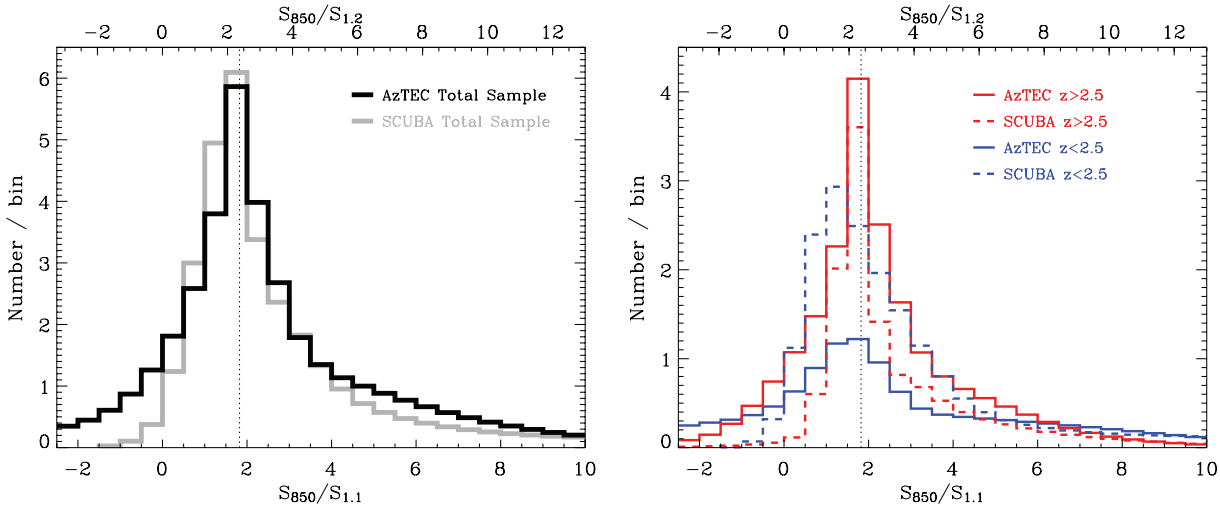

Figure 7. Histograms of the $R = S_{850}/S_{1.1}$ flux ratio. In each case, the vertical dotted line corresponds to a value of $R = 1.8$ calculated from high-S/N sources in Fig. 6. The top horizontal axes assume a $\beta = 1.5$, $T = 30$ K modified blackbody spectrum to predict the corresponding $S_{850}/S_{1.2}$ colours for comparison with MAMBO results. Left-hand panel: the black and grey histograms show the distributions of AzTEC and SCUBA selected sources, respectively. As in Fig. 5, the uncertainty of each object is convolved with its error distribution before placing it in the histogram, such that higher S/N measurements are more sharply peaked. Right-hand: here the samples have been divided into subsets above and below redshift $z = 2.5$. Although similar numbers of objects lie in each redshift bin, the higher redshift bin is dominated by the high-S/N detections of *AzGN* 1 and *AzGN* 1.2.

that this scatter is roughly symmetric: the 850 μm measurements fall above the expected values about as often as they fall below (in the left-hand panel of Fig. 6).

These calculations are biased to 1.1 mm selected sources, and could in principle be different for an 850 μm selected catalogue. We therefore repeat the procedure, starting with deboosted flux densities for the 20 robustly identified SCUBA sources mentioned in Section 3, scaling them to 1.1 mm by *dividing* them by *R*, and comparing these predictions to photometry at the locations of their counterparts in the AzTEC map (right-hand panel of Fig. 6). In this case, the scatter is clearly asymmetric, with a number of the SCUBA sources appearing fainter than expected in the AzTEC map. However, these outliers are primarily low-S/N SCUBA detections (indicated by the large horizontal error bars), in particular *GN* 3, *GN* 5, *GN* 7, *GN* 16 and *GN* 22 which have uncertainties ranging from 1.5–4.5 mJy. We hypothesize that the Pope et al. (2006) deboosting recipe did not sufficiently correct these sources, i.e. they should have been shifted further to the left in this plot. This explanation is plausible because their deboosting factors were extrapolated from those calculated for the SCUBA SHADES survey (Coppin et al. 2006), which were derived for sources with a different noise distribution. Furthermore, the fact that the AzTEC selected source list does not exhibit this problem (left-hand panel of Fig. 6) also points to an issue with the SCUBA deboosting calculation, rather than the map itself.

Finally, we use the AzTEC and SCUBA selected source lists to plot histograms of the measured $S_{850}/S_{1.1}$ flux ratios in Fig. 7. Here, we have convolved each source with its uncertainty distribution before adding it to the total histogram, so that higher S/N measurements are more sharply peaked and, therefore, contribute more to the shape. In the left-hand panel of this figure the resulting histograms for each sample are shown to be nearly indistinguishable, with modes that are coincident with the value $R = 1.8$ measured for the highest S/N detections in the AzTEC map (vertical dotted line). Since we also have redshift information, we split the samples into objects above and below $z = 2.5$, allowing us to search for a systematic trend. For the AzTEC selected sample, there is no significant difference in the ratios for low- and high-redshift objects. On the other hand, the mode of the SCUBA sample shows a mild trend to *higher* values of *R* with increasing redshift. However, given the evidence for incorrect deboosting of the SCUBA flux densities mentioned above, we do not believe this trend is significant.

From these measurements, we therefore conclude that there is no evidence for 850 μm dropouts in the 1.1 mm map. In fact, the observed trend in the $S_{850}/S_{1.1}$ colour tends to go in the opposite direction: AzTEC flux densities appear fainter than they should be starting with a SCUBA selected list (but not vice versa). How then can this result be reconciled with the measured shift in the AzTEC redshift distribution compared to SCUBA (Fig. 5), which can only be a result of enhanced brightness at 1.1 mm at larger values of *z*? Given the low-S/N measurements used here, the wavelength proximity of the 850 μm and 1.1 mm filters, and the fact that there appears to be a bias in the SCUBA flux densities from Pope et al. (2006), we believe that trends in the observed colour are completely obscured by uncertainties. Much deeper (and higher spectral resolution) observations would be needed to detect differences in the colours of 850 μm and 1.1 mm source populations.

4.3 Constraints on *T* and *β*

Given the $T-\beta$ degeneracy, low S/N and wavelength proximity of the SCUBA 850 μm and AzTEC 1.1 mm filters, the SED constraints for individual objects are extremely noisy. However, with this data set, it is possible to examine the constraints that we can place on the *family* of T and β consistent with the sample. Note that this is different to fitting SED templates based on objects in the local Universe using all of the available radio-IR photometry (e.g. Pope et al. 2006; Magnelli et al. 2009). The purpose of such fits is to give the best estimates of source properties, such as bolometric luminosities and star-formation/AGN fraction. However, the goal in this paper is to provide unbiased measurements that in the future may be used to constrain redshift-dependent SED libraries.

We have extracted a subset of the galaxies for which there are robust counterparts, 850 μm flux densities with a significance of

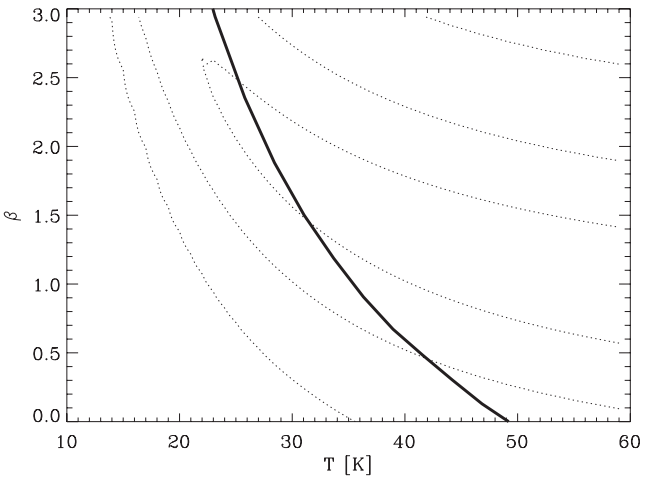

Figure 8. Dotted lines are contours in the joint likelihood function (0.6, 0.1 and 0.001 times the maximum likelihood) demonstrating the family of values for β and T consistent with a simultaneous fit to the five galaxies for which spectroscopic redshifts have been obtained, and there exist at least 3σ measurements of the 850 μm flux densities: *AzGN* 1, *AzGN* 1.2, *AzGN* 3, *AzGN* 7 and *AzGN* 16. The simple three-parameter rest-frame SED $A\nu^{\beta}B_{\nu}(T)$ is redshifted, and compared to the observed 850 μm and 1.1 mm flux densities for each object with a grid of parameter values, and then marginalized over A. The final two-dimensional likelihood surface is the product of the five individual marginalized distributions. The solid line is the locus of SEDs that produce the same peak in $S(\nu)$ as the best-fitting model from Coppin et al. (2008), $T = 31$ K and $\beta = 1.5$ such that we can see the effect of an additional shorter-wavelength measurement to reject the highest temperature/lowest β fits.

at least 3σ and spectroscopically measured redshifts: *AzGN* 1, *AzGN* 1.2, *AzGN* 7 and *AzGN* 16. We then plot the joint likelihood surface of the observed 850 μm and 1.1 mm flux densities given a range of models with T and β common to each object (marginalizing over the amplitudes A for each source as they are irrelevant to the joint distribution) in Fig. 8. This surface, as expected, produces a long anticorrelated valley between T and β. For comparison, we also plot the locus of SED models that would produce the same peak $S(\nu)$ as the best-fitting model from Coppin et al. (2008), $T = 31$ K assuming $\beta = 1.5$. As they use shorter-wavelength 350 μm follow-up of SMGs, the constraints are somewhat orthogonal to those described in this paper, showing the ability of observations at those wavelengths to reject the highest temperature and lowest β SEDs.

There is some evidence that this AzTEC sample lies at slightly higher redshift (Fig. 5), but the fact that we do not find significant '850 μm dropouts' suggests that, within the precision of the data, the SEDs are not different. At face value, Fig. 8 suggests that the best-fitting value at the intersection of the valley in the contour plot with the solid line occurs at $T \sim 30$ K and $\beta \sim 1.75$. However, it is clear that a large family of SEDs with temperatures ranging from $T \sim 25$ to 40 K and corresponding $\beta \sim 2$–1 are easily allowed.

5 CONCLUSIONS

We have used the rich multiwavelength data set in GOODS-N to identify robust radio and IR counterparts for sources detected at 1.1 mm using AzTEC. Of the 29 sources, only 1 or 2 are expected to be false positives. We find robust counterparts for 22 objects (false identification probabilities $P < 0.05$), although one object (*AzGN* 14/*HDF* 850.1) is dropped from the sample due to confusion about its identification, and tentative associations for the remaining eight objects are also provided. These counterparts have an astrometric precision of ∼1 arcsec, a significant improvement given the 18 arcsec FWHM AzTEC beam and low S/N.

We find spectroscopic redshifts for seven of the robustly identified sources in the literature, and provide photometric redshifts or limits for the remaining objects. Restricting ourselves to the 18 objects with robust counterparts and redshift estimates (spectroscopic or photometric, excluding limits), we measure a median $z = 2.7$, with an interquartile range 2.1–3.4. The 850 μm sources in this field, selected in a similar way, have a median redshift $z = 2.0$ with an interquartile range 1.3–2.6. We use K–S and M–W non-parametric tests to evaluate the significance of this shift to higher redshift in the 1.1 mm map, finding chance probabilities $p_{\rm KS} = 0.05$ and $p_{\rm MW} = 0.01$ that both surveys sample the same redshift population. Given the large uncertainties in individual photometric redshifts, we used Monte Carlo simulations to evaluate the spread in probabilities produced by the two tests consistent with our samples, finding $p_{\rm KS} < 0.15$ and $p_{\rm MW} < 0.04$ at a confidence level of 68 per cent.

For the entire overlapping region between the SCUBA and AzTEC maps, we perform unbiased flux density measurements in the SCUBA map at locations of identifications for AzTEC sources. Using the four most significant (3σ) detections in the two maps, we find a mean observed 850 μm to 1.1 mm flux density ratio $S_{850}/S_{1.1} = 1.8$. For the remaining 20 sources, we observe a symmetric scatter in the observed ratio which appears to be produced in equal quantities by intrinsic spread in spectral properties, and measurement noise. We also examine the ratios $S_{850}/S_{1.1}$ for objects selected at 850 μm, finding that they are also generally consistent with this value, although it appears that the lower S/N 850 μm flux densities may be biased high. Finally, we unsuccessfully searched for trends in this flux density ratio with redshift for both samples. We, therefore, do not see evidence for 850 μm dropouts in the 1.1 mm map as reported in Greve et al. (2004, 2008). While we believe that such a trend must exist in the underlying SMG population to produce the mild differences in the redshift distributions mentioned above, it is undetectable when comparing ∼4σ detections in wavelength bands that are so close to each other.

We test the hypothesis of a single temperature, T, and dust emissivity index, β, for the ensemble of sources having robust identifications and photometric redshift estimates. Given the degeneracy between these parameters (since we have only two photometric measurements at different wavelengths), we assume the same mean rest-frame far-IR peak as found in other studies, finding that $T = 30$ K and $\beta = 1.75$ are consistent with all of the data. However, given the S/N, these measurements still provide only a weak constraint, and data at shorter rest-frame far-IR wavelengths would be required to tighten up the allowable range of SEDs. SCUBA-2 450 μm, as well as Spectral and Photometric Imaging Receiver (SPIRE) and new Balloon-borne Large Aperture Submillimeter Telescope (BLAST) 250, 350 and 500 μm surveys (e.g. Devlin et al. 2009; Dye et al. 2009) should be particularly useful.

ACKNOWLEDGMENTS

We thank D. Stern, E. MacDonald and M. Dickinson for providing their unpublished Keck redshift for *AzGN* 27. We also thank the anonymous referees for their helpful comments. This research was supported by the Natural Sciences and Engineering Research Council of Canada, and the NSF grant AST05-40852. AP acknowledges support provided by NASA through the *Spitzer* Space Telescope Program, through a contract issued by the Jet Propulsion

Laboratory, California Institute of Technology under a contract with NASA. IA and DHH acknowledge partial support by CONACyT from research grants 39953-F and 39548-F.

REFERENCES

Alexander D. M., Bauer F. E., Chapman S. C., Smail I., Blain A. W., Brandt W. N., Ivison R. J., 2005, ApJ, 632, 736
Almaini O. et al., 2003, MNRAS, 338, 303
Aretxaga I. et al., 2007, MNRAS, 379, 1571
Austermann J. E. et al., 2009, MNRAS, submitted (arXiv:0907.1093)
Barger A. J., Cowie L. L., Sanders D. B., Fulton E., Taniguchi Y., Sato Y., Kawara K., Okuda H., 1998, Nat, 394, 248
Barger A. J., Cowie L. L., Richards E. A., 2000, AJ, 119, 2092
Barger A. J., Cowie L. L., Wang W.-H., 2008, ApJ, 689, 687
Bautz M. W., Malm M. R., Baganoff F. K., Ricker G. R., Canizares C. R., Brandt W. N., Hornschemeier A. E., Garmire G. P., 2000, ApJ, 543, L119
Bertoldi F. et al., 2007, ApJS, 172, 132
Blain A. W., Smail I., Ivison R. J., Kneib J.-P., Frayer D. T., 2002, Phys. Rev., 369, 111
Borys C., Chapman S. C., Halpern M., Scott D., 2002, MNRAS, 330, L63
Borys C., Chapman S., Halpern M., Scott D., 2003, MNRAS, 344, 385
Borys C., Scott D., Chapman S., Halpern M., Nandra K., Pope A., 2004, MNRAS, 355, 485
Carilli C. L., Yun M. S., 1999, ApJ, 513, L13
Chapman S. C., Blain A. W., Smail I., Ivison R. J., 2005, ApJ, 622, 772
Cohen J. G., Hogg D. W., Blandford R., Cowie L. L., Hu E., Songaila A., Shopbell P., Richberg K., 2000, ApJ, 538, 29
Coppin K., Halpern M., Scott D., Borys C., Chapman S., 2005, MNRAS, 357, 1022
Coppin K. et al., 2006, MNRAS, 372, 1621
Coppin K. et al., 2008, MNRAS, 384, 1597
Cowie L. L., Barger A. J., Kneib J.-P., 2002, AJ, 123, 2197
Cowie L. L., Barger A. J., Hu E. M., Capak P., Songaila A., 2004, AJ, 127, 3137
Cowie L. L., Barger A. J., Wang W.-H., Williams J. P., 2009, ApJ, 697, L122
Daddi E. et al., 2009a, ApJ, 694, 1517
Daddi E., Dannerbauer H., Krips M., Walter F., Dickinson M., Elbaz D., Morrison G. E., 2009b, ApJ, 695, L176
Devlin M. J. et al., 2009, Nat, 458, 737
Downes A. J. B., Peacock J. A., Savage A., Carrie D. R., 1986, MNRAS, 218, 31
Dunlop J. S. et al., 2004, MNRAS, 350, 769
Dye S., Ade P. A. R., Bock J. J., Chapin E. L., Devlin M. J., Dunlop J. S., Eales S. A., 2009, ApJ, in press
Eales S., Lilly S., Gear W., Dunne L., Bond J. R., Hammer F., Le Fèvre O., Crampton D., 1999, ApJ, 515, 518
Eales S., Bertoldi F., Ivison R., Carilli C., Dunne L., Owen F., 2003, MNRAS, 344, 169
Greve T. R., Ivison R. J., Bertoldi F., Stevens J. A., Dunlop J. S., Lutz D., Carilli C. L., 2004, MNRAS, 354, 779
Greve T. R., Pope A., Scott D., Ivison R. J., Borys C., Conselice C. J., Bertoldi F., 2008, MNRAS, 389, 1489
Hildebrand R. H., 1983, QJRAS, 24, 267
Hornschemeier A. E. et al., 2000, ApJ, 541, 49
Hughes D. H. et al., 1998, Nat, 394, 241
Huynh M. T., Pope A., Frayer D. T., Scott D., 2007, ApJ, 659, 305
Iono D. et al., 2006, ApJ, 640, L1
Ivison R. J. et al., 2002, MNRAS, 337, 1
Ivison R. J. et al., 2007, MNRAS, 380, 199
Khan S. A. et al., 2007, ApJ, 665, 973
Knudsen K. K. et al., 2006, MNRAS, 368, 487
Kovács A., Chapman S. C., Dowell C. D., Blain A. W., Ivison R. J., Smail I., Phillips T. G., 2006, ApJ, 650, 592
Laurent G. T. et al., 2005, ApJ, 623, 742
Magnelli B., Elbaz D., Chary R. R., Dickinson M., Le Borgne D., Frayer D. T., Willmer C. N. A., 2009, A&A, 496, 57
Perera T. A. et al., 2008, MNRAS, 391, 1227
Pope E. A., 2007, PhD thesis, Univ. British Columbia
Pope A., Borys C., Scott D., Conselice C., Dickinson M., Mobasher B., 2005, MNRAS, 358, 149
Pope A. et al., 2006, MNRAS, 370, 1185
Pope A. et al., 2008, ApJ, 675, 1171
Reddy N. A., Steidel C. C., Erb D. K., Shapley A. E., Pettini M., 2006, ApJ, 653, 1004
Richards E. A., 2000, ApJ, 533, 611
Sanders D. B., Mirabel I. F., 1996, ARA&A, 34, 749
Sawicki M., 2002, AJ, 124, 3050
Scott S. E. et al., 2002, MNRAS, 331, 817
Scott K. S. et al., 2008, MNRAS, 385, 2225
Serjeant S. et al., 2003, MNRAS, 344, 887
Simpson C., Eisenhardt P., 1999, PASP, 111, 691
Smail I., Ivison R. J., Blain A. W., 1997, ApJ, 490, L5
Smail I., Ivison R. J., Blain A. W., Kneib J.-P., 2002, MNRAS, 331, 495
Swinbank A. M., Smail I., Chapman S. C., Blain A. W., Ivison R. J., Keel W. C., 2004, ApJ, 617, 64
Wall J. V., Pope A., Scott D., 2008, MNRAS, 383, 435
Wang W.-H., Cowie L. L., Barger A. J., 2004, ApJ, 613, 655
Webb T. M. et al., 2003, ApJ, 587, 41
Wilson G. W. et al., 2008a, MNRAS, 386, 807
Wilson G. W., Hughes D. H., Aretxaga I., Ezawa H., Austermann J. E., Doyle S., Ferrusca D., 2008b, MNRAS, 390, 1061
Wirth G. D. et al., 2004, AJ, 127, 3121
Younger J. D. et al., 2007, ApJ, 671, 1531
Yun M. S. et al., 2008, MNRAS, 389, 333

APPENDIX A: DATA TABLES

Here, we provide proposed identifications and multiwavelength photometry for all of the sources. Table A1 provides updated positions and raw map flux densities for AzTEC 1.1 mm sources that required deblending. Tables A2 and A3 summarize the identifications and SEDs, respectively.

APPENDIX B: NOTES ON EACH SOURCE

This section gives detailed information on each source not provided in the tables of Appendix A.

B1 Robust identifications

Sources in this category have potential counterparts with $P < 0.05$ within 6 arcsec.

AzGN 1: *GN* 20 from Pope et al. (2006). This source has been deblended from *AzGN* 1.2 (see Table A1), and the submm emission was also localized using the SMA (Iono et al. 2006). A spectroscopic redshift of 4.055 for this source was reported in Daddi et al.

Table A1. New source positions and raw 1.1 mm map flux densities resulting from simultaneous two-source fits. Source Az 1.2 is a new object in this paper, whereas the other three were originally detected in AzTEC maps in Perera et al. (2008).

AzTEC ID	RA ($^{h\ m\ s}$)	Dec. ($^{\circ\ \prime\ \prime\prime}$)	Map flux density (mJy)
1	12 37 11.99	+62 22 11.1	12.73 ± 0.99
1.2	12 37 09.15	+62 22 02.1	4.14 ± 0.98
14	12 36 52.23	+62 12 25.2	4.11 ± 0.97
22	12 36 49.12	+62 12 13.1	4.56 ± 0.97

Table A2. Radio and *Spitzer* identifications of AzTEC sources (procedure described in Section 2). Counterpart distances in brackets employed a 10 arcsec search radius. *P* values in boldface emphasize robust counterparts with values <0.05. Spectroscopic redshifts are given in the column labelled $z_{\rm spec}$ (references for these measurements given in Appendix B). Photometric redshifts based on *Spitzer* IR flux densities from Table A3 are calculated using equation (2) from Pope et al. (2006) and given in the penultimate column, $z_{\rm ir}$. These redshifts have uncertainties $\Delta\, z_{\rm ir} = 0.15(1 + z)$, and are biased low at $z > 3$. Photometric redshifts based on the (sub)mm-to-radio colours are given in the last column, $z_{\rm rm}$. The quoted 68 per cent uncertainties are theoretically derived; in this paper, we assume an empirically measured symmetric error $\Delta\, z_{\rm rm} = 0.8$.

AzTEC	SCUBA	Radio			Spitzer				Redshift		
ID	ID	RA ($^{\rm h\ m\ s}$)	Dec. ($^\circ\ '\ ''$)	Dist. ($''$)	RA ($^{\rm h\ m\ s}$)	Dec. ($^\circ\ '\ ''$)	Dist. ($''$)	*P*	$z_{\rm spec}$	$z_{\rm ir}$	$z_{\rm rm}$
1	20	12 37 11.88	+62 22 11.8	1.0	12 37 11.88	+62 22 12.1	1.3	**0.003**	**4.055**	2.7	$3.8^{+1.2}_{-0.7}$
1.2	20.2	12 37 08.78	+62 22 01.8	2.6	12 37 08.77	+62 22 01.8	2.7	**0.005**	**4.052**	2.5	$3.1^{+1.2}_{-0.2}$
		12 37 09.73	+62 22 02.5	4.1	12 37 09.57	+62 22 02.1	2.9	**0.037**	...	3.1	$2.5^{+0.8}_{-0.8}$
2	...	12 36 31.93	+62 17 14.7	5.3	12 36 31.92	+62 17 14.6	5.2	0.051	...	3.2	$2.4^{+2.3}_{-0.1}$
3	10	12 36 33.42	+62 14 08.7	0.6	12 36 33.40	+62 14 08.4	0.6	**0.002**	**4.042**	2.3	$3.1^{+1.4}_{-0.2}$
4	...	12 35 50.26	+62 10 41.3	3.1	12 35 50.35	+62 10 41.8	2.7	**0.030**[a]	...	2.9	$2.4^{+2.2}_{-0.2}$
5	...	12 37 30.78	+62 12 58.7	2.6	12 37 30.75	+62 12 58.4	2.2	**0.007**	...	2.0	$2.1^{+1.6}_{-0.9}$
6	...	12 36 27.26	+62 06 05.7	1.6	12 36 27.21	+62 06 05.7	1.2	**0.007**	...	3.0	$2.9^{+1.4}_{-1.1}$
7	39	12 37 11.32	+62 13 30.9	4.4	12 37 11.34	+62 13 31.0	4.3	**0.014**	**1.996**	1.7	$2.7^{+0.9}_{-0.8}$
		12 37 11.99	+62 13 25.6	4.5	12 37 11.99	+62 13 25.7	4.4	**0.032**	**1.992**	2.0	>2.3
8	12	12 36 46.04	+62 14 48.6	(6.9)	12 36 46.07	+62 14 48.8	(7.0)	**0.037**	...	2.0	$3.0^{+0.6}_{-1.0}$
		12 36 46.80	+62 14 45.3	(7.5)	12 36 46.88	+62 14 47.2	(9.0)	**0.050**	**2.006**	0.7	$2.9^{+0.7}_{-1.1}$
9	37	12 37 38.16	+62 17 37.0	1.6	12 37 38.26	+62 17 36.4	0.9	**0.013**	**3.1900**	2.4	>3.0
10	...	12 36 27.54	+62 12 17.8	3.5	12 36 27.48	+62 12 18.0	3.1	0.066[a]	...	3.0	$2.1^{+2.2}_{-0.7}$
11	27	12 36 35.89	+62 07 03.8	3.1				**0.027**	...	...	$2.8^{+1.3}_{-0.2}$
12	...	12 36 32.65	+62 06 21.1	4.7	12 36 32.65	+62 06 21.3	4.9	**0.047**	...	2.8	>1.3
13	...	12 35 54.23	+62 13 43.8	2.9	12 35 54.28	+62 13 43.4	3.3	**0.033**[a]	...	2.2	$2.6^{+0.9}_{-1.5}$[c]
14	14	12 36 52.07[d]	+62 12 25.7[d]	1.2					...	...	...
15	...	12 35 47.93	+62 15 29.2	5.0	12 35 48.09	+62 15 29.3	3.9	**0.018**	...	...	>1.6
					12 35 47.87	+62 15 28.2	5.7		...	...	>1.6
16	04	12 36 16.09	+62 15 13.8	4.3	12 36 16.10	+62 15 13.6	4.5	**0.038**	**2.578**	2.0	$2.4^{+2.1}_{-0.2}$
		12 36 15.80	+62 15 15.1	4.0	12 36 15.82	+62 15 15.4	3.6	**0.039**	...	4.5	$3.0^{+0.3}_{-0.2}$
17	...	12 35 39.92	+62 14 42.1	(7.6)	12 35 39.95	+62 14 40.8	(6.5)	0.062	...	...	>1.7
		12 35 39.91	+62 14 30.8	(7.1)	12 35 39.97	+62 14 30.7	(6.9)	0.067	...	...	>1.7
					12 35 39.76	+62 14 30.7	(7.9)		...	...	>1.7
18	38	12 37 41.16	+62 12 20.5	3.8	12 37 41.16	+62 12 20.9	3.5	**0.032**	...	2.1	$2.4^{+0.6}_{-2.0}$
		12 37 41.63	+62 12 23.6	5.8	12 37 41.66	+62 12 23.6	6.0	0.051	...	2.0	>2.2[c]
19	...	12 36 04.40	+62 07 02.7	2.6	12 36 04.43	+62 07 02.9	2.8	**0.022**	...	...	>1.5
20	...	12 37 12.48	+62 10 35.4	3.0	12 37 12.51	+62 10 35.6	2.8	**0.030**	...	3.3	>2.3
21	...	12 38 00.80	+62 16 11.7	1.5	12 38 00.81	+62 16 11.7	1.4	**0.016**[a]	...	2.3	>1.6
22	...	12 36 48.60	+62 12 16.1	4.7	12 36 48.65	+62 12 15.7	4.2	0.083[a]	...	1.7	>0.7
23	...	12 37 16.67	+62 17 33.2	1.4	12 37 16.67	+62 17 33.3	1.4	**0.001**	**1.1460**	1.6	>1.8
24	23	12 36 08.58	+62 14 35.3	(6.4)	12 36 08.60	+62 14 35.3	(6.4)	0.079	...	2.7	$2.4^{+2.0}_{-0.8}$
25	...	12 36 51.72	+62 05 03.0	4.1				**0.021**	...	...	>0.7
26	40	12 37 13.86	+62 18 26.2	0.6	12 37 13.85	+62 18 26.2	0.5	**0.000**	...	2.6	>0.7
27	...	12 37 19.62	+62 12 20.3	1.3	12 37 19.61	+62 12 20.9	0.9	**0.034**[b]	...	3.1	>0.7
		12 37 20.01	+62 12 22.0	2.1	12 37 19.99	+62 12 22.6	2.2	**0.050**[b]	**2.4600**	2.0	>0.7
28	...	12 36 44.03	+62 19 38.8	4.2	12 36 44.03	+62 19 38.4	3.9	0.071[a]	...	2.5	>0.7

[a]Identified in 3σ radio catalogue.
[b]Identified in MIPS 24 μm catalogue.
[c]Photometric redshift calculation excludes extremely noisy 850 μm photometry.
[d]Position for *HDF* 850.1 from Dunlop et al. (2004). See also Cowie et al. (2009).

(2009a) based on molecular CO emission detected with the Institut de Radioastronomie Millimétrique (IRAM) Plateau de Bure Interferometer (PdBI), with some confirmation based on optical spectroscopy in Pope (2007).

AzGN 1.2: this was already known to be a second component of *AzGN* 1 from the SCUBA data. In the AzTEC map, the source was deblended by performing a simultaneous fit of two scaled effective PSFs using the peak at the location of *AzGN* 1 and the position of

Table A3. Photometry data listed in the same order as the identifications in Table A2. The 850 μm flux densities are measured directly from the SCUBA map of Pope et al. (2006) at the positions of each proposed counterpart, and should therefore be unbiased at each correct position. 24 μm upper limits are given at a significance of 3σ. Deboosted AzTEC 1.1 mm flux densities are taken from Perera et al. (2008) except for *AzGN* 1, *AzGN* 1.2, *AzGN* 14 and *AzGN* 22, which are calculated using the raw map flux densities from Table A1, but adopting the same prior.

AzTEC ID	1.4 GHz (μJy)	1.1 mm (mJy)	850 μm (mJy)	24 μm (μJy)	8 μm (μJy)	5.8 μm (μJy)	4.5 μm (μJy)	3.6 μm (μJy)
1	72.8 ± 12.3	$11.81 \pm^{+1.18}_{-1.07}$	20.30 ± 2.10	65.5 ± 4.5	25.3 ± 1.5	15.9 ± 1.3	9.2 ± 0.8	6.8 ± 0.6
1.2	173.5 ± 6.3	$2.87 \pm^{+1.25}_{-1.25}$	9.90 ± 2.30	20.2 ± 3.5	9.4 ± 1.1	6.1 ± 1.0	3.9 ± 0.5	3.9 ± 0.6
	35.2 ± 6.3		9.90 ± 2.30	12.9 ± 3.1	14.9 ± 1.5	11.8 ± 1.3	9.8 ± 0.8	8.0 ± 0.9
2	26.2 ± 4.6	$5.91 \pm^{+1.02}_{-1.00}$	5.74 ± 2.81	37.7 ± 4.8	24.9 ± 1.5	17.0 ± 1.3	10.9 ± 0.8	6.4 ± 0.6
3	36.0 ± 4.2	$5.35 \pm^{+0.94}_{-1.08}$	10.50 ± 1.59	26.2 ± 5.1	5.1 ± 1.1	2.7 ± 0.9	2.0 ± 0.4	1.2 ± 0.4
4	34.1 ± 10.7	$4.69 \pm^{+1.06}_{-1.06}$	...	92.5 ± 4.2	37.0 ± 1.7	26.0 ± 1.5	16.0 ± 0.8	9.6 ± 0.9
5	128.2 ± 8.0	$4.13 \pm^{+1.08}_{-0.98}$	4.37 ± 3.92	181.0 ± 6.5	28.9 ± 1.7	18.9 ± 1.3	12.7 ± 0.8	9.2 ± 0.9
6	58.5 ± 13.1	$4.13 \pm^{+1.12}_{-1.00}$	...	11.3 ± 8.3	9.9 ± 1.1	4.1 ± 1.0	2.5 ± 0.4	1.7 ± 0.4
7	127.3 ± 8.6	$3.95 \pm^{+1.08}_{-0.98}$	6.61 ± 1.89	537.0 ± 9.3	37.8 ± 1.7	53.3 ± 1.5	45.0 ± 1.0	37.9 ± 1.2
	51.6 ± 8.2		7.47 ± 2.35	219.0 ± 6.6	12.3 ± 1.5	16.1 ± 1.3	11.4 ± 0.8	9.2 ± 0.9
8	120.0 ± 7.6	$3.83 \pm^{+1.08}_{-1.00}$	7.83 ± 1.29	145.0 ± 12.2	13.8 ± 1.5	11.2 ± 1.3	7.9 ± 0.8	5.7 ± 0.6
	94.3 ± 11.8		5.50 ± 1.07	422.0 ± 29.1	27.8 ± 1.7	29.8 ± 1.5	31.7 ± 1.0	44.6 ± 1.2
9	26.0 ± 5.4	$3.39 \pm^{+1.02}_{-1.10}$	5.65 ± 2.38	32.2 ± 5.0	9.2 ± 1.1	8.5 ± 1.0	6.6 ± 0.5	6.2 ± 0.6
10	17.9 ± 4.3	$3.35 \pm^{+1.02}_{-1.10}$	2.25 ± 1.95	22.1 ± 6.8	9.7 ± 1.1	4.2 ± 1.0	2.3 ± 0.4	1.2 ± 0.4
11	36.2 ± 10.2	$3.27 \pm^{+1.08}_{-1.08}$	10.94 ± 4.60	...	22.0 ± 2.0	10.5 ± 2.0	5.6 ± 1.5	4.6 ± 1.5
12	26.6 ± 5.2	$3.07 \pm^{+1.12}_{-1.08}$	4.42 ± 8.50	29.7 ± 8.8	7.9 ± 1.1	4.7 ± 1.0	2.4 ± 0.4	1.6 ± 0.4
13	28.9 ± 12.1	$3.07 \pm^{+1.10}_{-1.12}$	16.49 ± 4.64	154.0 ± 6.3	19.6 ± 1.5	21.9 ± 1.3	16.4 ± 0.8	12.8 ± 0.9
14	...	$2.87 \pm^{+1.25}_{-1.25}$	5.88 ± 0.33	...	...	...	...	...
15	123.4 ± 5.5	$3.23 \pm^{+1.26}_{-1.32}$	...	<65.1	6.7 ± 1.1	14.7 ± 1.3	7.1 ± 0.5	2.4 ± 0.4
	...		...	<65.1	10.9 ± 1.5	13.6 ± 1.3	7.5 ± 0.5	2.6 ± 0.4
16	37.8 ± 8.2	$2.89 \pm^{+1.08}_{-1.14}$	5.75 ± 0.98	326.0 ± 8.0	43.4 ± 1.7	29.5 ± 1.5	18.1 ± 0.8	12.3 ± 0.9
	29.9 ± 9.2		5.38 ± 0.98	4.8 ± 7.2	27.1 ± 1.7	27.9 ± 1.5	19.5 ± 0.8	14.9 ± 0.9
17	80.7 ± 11.8	$3.23 \pm^{+1.24}_{-1.42}$	...	<24.0	13.3 ± 1.5	15.7 ± 1.3	8.1 ± 0.8	2.0 ± 0.4
	66.2 ± 5.8		...	<59.4	6.9 ± 1.1	14.4 ± 1.3	10.5 ± 0.8	8.6 ± 0.9
	...		...	<58.5	11.9 ± 1.5	13.5 ± 1.3	8.2 ± 0.8	5.8 ± 0.6
18	38.3 ± 9.0	$2.79 \pm^{+1.16}_{-1.08}$	18.97 ± 6.56	127.0 ± 5.8	23.1 ± 1.5	14.4 ± 1.3	10.3 ± 0.8	6.6 ± 0.6
	32.2 ± 5.0		24.17 ± 6.57	111.0 ± 4.6	16.4 ± 1.5	11.1 ± 1.3	7.8 ± 0.8	5.9 ± 0.6
19	34.4 ± 5.6	$3.07 \pm^{+1.20}_{-1.36}$	15.03 ± 8.30	< 9.0	42.7 ± 1.7	47.0 ± 1.5	31.8 ± 1.0	46.6 ± 1.2
20	26.6 ± 4.4	$2.79 \pm^{+1.08}_{-1.16}$	3.98 ± 1.53	35.1 ± 5.7	16.6 ± 1.5	14.3 ± 1.3	8.9 ± 0.8	5.5 ± 0.6
21	23.0 ± 5.7	$2.65 \pm^{+1.16}_{-1.16}$	6.29 ± 4.47	182.0 ± 6.2	24.7 ± 1.5	37.1 ± 1.5	34.1 ± 1.0	26.5 ± 1.2
22	18.9 ± 4.3	$3.35 \pm^{+1.22}_{-1.02}$	0.29 ± 0.40	291.0 ± 7.4	24.0 ± 1.5	32.4 ± 1.5	32.0 ± 1.0	27.3 ± 1.2
23	381.2 ± 8.2	$2.39 \pm^{+1.16}_{-1.18}$	-4.18 ± 3.56	1240.0 ± 15.5	239.6 ± 1.7	129.3 ± 1.5	83.5 ± 1.0	62.7 ± 1.2
24	44.6 ± 8.6	$2.39 \pm^{+1.18}_{-1.20}$	5.54 ± 1.74	51.1 ± 5.8	18.3 ± 1.5	13.4 ± 1.3	9.5 ± 0.8	6.4 ± 0.6
25	79.2 ± 5.6	$2.55 \pm^{+1.32}_{-1.42}$	...	...	...	...	...	...
26	651.8 ± 5.0	$2.39 \pm^{+1.10}_{-1.28}$	11.53 ± 2.43	55.2 ± 5.8	16.6 ± 1.5	9.4 ± 1.3	6.0 ± 0.5	3.5 ± 0.6
27	10.1 ± 8.1	$2.31 \pm^{+1.16}_{-1.22}$	0.27 ± 2.09	31.2 ± 6.7	22.4 ± 1.5	20.2 ± 1.3	15.5 ± 0.8	11.7 ± 0.9
	20.2 ± 10.8		1.18 ± 2.19	141.0 ± 7.3	17.7 ± 1.5	17.1 ± 1.3	12.9 ± 0.8	10.7 ± 0.9
28	20.8 ± 5.4	$2.31 \pm^{+1.14}_{-1.30}$	12.80 ± 8.66	29.9 ± 5.9	10.2 ± 1.1	4.8 ± 1.0	4.1 ± 0.5	2.1 ± 0.4

GN 20.2 from Pope et al. (2006) as starting values (see Table A1). Positions and flux densities were then allowed to vary (a total of six parameters). The reduced χ^2 for this fit decreased to 0.99 from 1.15 when only a single source was used, justifying the addition of the extra parameters. This procedure yields a clear 4.2σ source which corresponds to *GN* 20.2 from Pope et al. (2006). There are two possible radio identifications, one fainter object is 4.1 arcsec away with $P = 0.037$, and the other brighter source is 2.6 arcsec away with $P = 0.005$. The brighter object is the claimed counterpart to *AzGN* 1.2 from Pope et al. (2006). However, both potential counterparts mentioned here are also discussed in Daddi et al. (2009a). They detect a faint emission line from the brighter radio source which they argue to be consistent with molecular CO emission at a redshift 4.051. We concur with Daddi et al. (2009a) that the brighter object is likely an AGN, based on its relatively large radio/mm flux ratio.

AzGN 3: the AzTEC detection, and proposed counterpart, are both coincident with the SCUBA source *GN* 10 and identification from Pope et al. (2006). Similar to *AzGN* 1 and *AzGN* 1.2, Daddi

et al. (2009b) identified a spectroscopic redshift of 4.042 using CO emission detected with the IRAM PdBI.

AzGN 4: there is a single unambiguous radio counterpart.

AzGN 5: there is a single unambiguous radio counterpart. This object is not part of the Pope et al. (2006) catalogue (probably because of the high noise in this region), but was originally discovered in the SCUBA jiggle map of Wang et al. (2004) (GOODS 850–6). Our proposed counterpart corresponds to object 'c' from their analysis. We note a large discrepancy between the 850 μm flux density of this source at the coordinates of the proposed counterpart in the *Hubble Deep Field* (HDF) supermap, 4.4 ± 3.9 mJy, used in this paper (Table A3), compared with 19.41 ± 3.2 mJy from Wang et al. (2004) which is due at least in part to the lack of correction for Eddington bias in that work. Based on the 1.1 mm flux density and our measured ratio $S_{850}/S_{1.1} = 1.8$, we would expect $S_{850} \simeq 7$ mJy.

AzGN 6: there is a single unambiguous radio counterpart.

AzGN 7: this object is also a significant SCUBA source, *GN* 39, described in Wall et al. (2008). We find the same two radio identifications with spectroscopic redshifts 1.996 (Chapman et al. 2005) and 1.992 (Swinbank et al. 2004), respectively.

AzGN 9: this object is also a significant SCUBA source, *GN* 37 from Pope et al. (2006) for which we find the same identification with spectroscopic redshift 3.190 (Cowie et al. 2004).

AzGN 11: this object is close to the SCUBA source *GN* 27 from Pope et al. (2006) that is classified as 'tentative' since it does not exceed their threshold for posterior deboosted flux density probability above 0. There appear to be three distinct peaks in the radio map that fall between the SCUBA and AzTEC peaks (but closer to the AzTEC position). Two of these peaks are coincident with *Spitzer* sources at redshifts 0.56 and 0.276. The ACS/IRAC counterpart to *GN* 27 claimed in Pope et al. (2006) is to the south of the three objects that we find, and is not a significant source in our 1.4 GHz map. The third source is considerably fainter and redder in the IRAC channels. However, due to blending with the other sources, we are unable to produce the SED at *Spitzer* wavelengths in Table A3. We rule out the low-z identifications based on their highly unlikely SEDs which would exhibit extraordinarily low radio/(sub)mm flux density ratios.

AzGN 12: there is a single unambiguous radio counterpart.

AzGN 13: there is a single unambiguous radio counterpart within 6 arcsec. We note that there are two radio sources 7.9 arcsec (12:35:53.90 +62:13:37.1) and 8.7 arcsec (12:35:53.24 +62:13:37.5) to the south that are coincident with a low-significance peak of SCUBA emission. The second source was also part of the Chapman et al. (2005) sample. While they are not considered likely in our analysis, we list them here for completeness. Had we used a search radius of 10 arcsec, they would have P values of 0.103 and 0.108, and lie at redshifts 0.8770 (Reddy et al. 2006) and 2.098 (Chapman et al. 2005; Reddy et al. 2006), respectively.

AzGN 14: this object is *HDF* 850.1, the highest S/N SMG from the HDF-N map of Hughes et al. (1998). Similar to the case for *AzGN* 1 and *AzGN* 1.2, this source has been deblended from *AzGN* 22 (see Table A1). Various counterparts have been suggested, with two detailed studies giving different answers. Dunlop et al. (2004) subtract the emission from an elliptical galaxy that is believed to obscure a faint background K-band counterpart at 12:36:52.07 + 62:12:25.7 (this position is given in Table A2). Recently, Cowie et al. (2009) used the SMA to localize the source of the submm emission to 12:36:51.99 + 62:12:25.83, concluding that this position is incompatible with the Dunlop et al. (2004) counterpart. For the purposes of measuring unbiased flux densities in the SCUBA and AzTEC maps, either position may be used as the differences are small compared to the (sub)mm beams. Had we applied our counterpart search blindly, we would have instead chosen a more distant radio source at 12:36:51.72 + 62:12:21.36 ($P = 0.036$), although we would have rejected this counterpart based on the unrealistic SED. This case demonstrates the potential for counterparts identified with low values of P to be misleading. No *Spitzer* flux densities are quoted for this special source, and it is excluded from most of the analysis in this paper.

AzGN 15: there is a single unambiguous radio counterpart, although it appears to resolve into two objects in the *Spitzer* catalogue. Inspection of the map shows, however, that these data lie at the extreme edge of the *Spitzer* coverage, and we suspect that the two sets of photometry are in fact for the same source.

AzGN 16: similar to *AzGN* 7, this object is also detected with SCUBA (*GN* 4 from Pope et al. 2006), and has two radio counterparts. The more distant counterpart has a spectroscopic redshift of 2.578 (Chapman et al. 2005).

AzGN 18: this object is also a significant SCUBA source, *GN* 38 from Pope et al. (2006), and we find the same two radio counterparts. One of these counterparts technically misses the significance threshold with $P = 0.051$, but lies very close to the centre of the SCUBA emission peak. Conversely, the other object, with $P = 0.032$, lies closer to the peak of the AzTEC emission. The photometric redshifts for both sources are consistent with them being at the same distance.

AzGN 19: there is a single unambiguous radio counterpart, and the position is coincident with a region of faint SCUBA emission. It falls off the edge of the MIPS 24 μm coverage, but within the IRAC footprint. There is a bright optical source within 1 arcsec of the radio position at $z = 0.65$. However, we reject this redshift and SED combination as it would imply an extraordinarily low radio/(sub)mm flux ratio. Therefore, the radio identification proposed here may be incorrect and *AzGN* 19 is associated with the low-z optical source instead, or it is correct and unrelated to the optical source. Since the (sub)mm/radio photometric redshift estimate is consistent with a more typical SMG ($z_{\rm rm} > 1.5$), we prefer the first hypothesis.

AzGN 20: there is a single unambiguous radio counterpart, and the position is coincident with a region of faint SCUBA emission.

AzGN 21: there is a single unambiguous radio counterpart.

AzGN 23: there is a single unambiguous radio counterpart. This object has the lowest spectroscopic redshift in the sample, $z = 1.146$ (Cowie et al. 2004).

AzGN 25: this object has a single clear radio counterpart, but lies beyond the *Spitzer* IRAC coverage. The MIPS 24 μm image exhibits emission at the location of the radio counterpart, but is not part of the *Spitzer* catalogue produced by the GOODS team.

AzGN 26: this object is also a significant SCUBA source, *GN* 40 from Wall et al. (2008). There is a single unambiguous radio identification.

AzGN 27: this source is coincident with faint SCUBA emission. There are no radio sources with $P < 0.05$, even searching out to 10 arcsec. However, there are two MIPS 24 μm sources 0.9 and 2.2 arcsec away, with P values 0.034 and 0.05, respectively. The more distant source has a spectroscopic redshift $z = 2.460$ (Stern et al. in preparation), and photometric redshift estimates for the other source are broadly consistent with this value. As this object appears to have an extraordinarily faint radio flux density given the 24 μm measurement, we warn the reader that these identifications may be suspect.

B2 Other identifications

For the remaining sources, we give our best estimates for the counterparts, considering objects with $0.05 < P < 0.10$ and/or searching out to 10 arcsec from the AzTEC positions.

AzGN 2: there is a radio source 5.3 arcsec to the north that slightly misses the significance cut ($P = 0.051$). This proposed counterpart is in the direction of a faint 2σ signal in the SCUBA map.

AzGN 8: this object is also a significant SCUBA source, *GN* 12. There are two potential radio counterparts 7 and 9 arcsec away. Had we used a search radius of 10 arcsec, the values of P would have been 0.037 and 0.050. Since the closer object would then have a lower P, and is also closer to the SCUBA peak, we prefer it as the most likely candidate, although strictly based on the 1.1 mm and 1.4 GHz emission, they are both reasonable candidates. Pope et al. (2006) were unable to obtain an optical spectrum for the nearer candidate. The other candidate was detected serendipitously with Keck at a redshift $z = 2.006$. This second object was rejected by Pope et al. (2006) based on its distance from the SCUBA centroid, and the unlikely rest-frame UV emission that would be uncharacteristic of a dusty star-forming galaxy.

AzGN 10: this object has a single potential radio counterpart within 6 arcsec, and is also coincident with faint SCUBA emission.

AzGN 17: this object is at the edge of the MIPS 24 μm coverage, but within the IRAC footprint. There are two potential radio counterparts at distances 7.1 and 7.6 arcsec.

AzGN 22: this source lies on a region of extended emission to the southeast of *AzGN* 14, which is also seen in the SCUBA map. To reduce the effect of blending with *AzGN* 14, we have performed a simultaneous two-object fit, as with *AzGN* 1 and *AzGN* 1.2 (resulting positions and map flux densities given in Table A1). The most likely counterpart, given the resulting centroid, is a radio source 4.7 arcsec away.

AzGN 24: there is a single potential radio counterpart 6.4 arcsec to the south. We consider this a likely identification because it falls between the AzTEC peak, and the SCUBA source *GN* 23 (Pope et al. 2006), for which the same identification was proposed.

AzGN 28: this object has a single potential radio counterpart 4.2 arcsec away, and is coincident with faint SCUBA emission. It has a redshift estimate $z_{\rm ir} = 2.5$.

This paper has been typeset from a TEX/LATEX file prepared by the author.